What Can Infrared Spectra Tell Us about the Crystallinity of Nanosized Interstellar Silicate Dust Grains?

(Article begins on next page)

18 October 2024

WHAT CAN INFRARED SPECTRA TELL US ABOUT THE CRYSTALLINITY OF NANO-SIZED INTERSTELLAR SILICATE DUST GRAINS?

Lorenzo Zamirri,[1],[§] Antoni Macià Escatllar,[2],[§] Joan Mariñoso Guiu,[2] Piero Ugliengo,[1],[*] and Stefan T. Bromley.[2],[3],[*]

[1] Dipartimento di Chimica and Nanostructured Interfaces and Surfaces (NIS) Centre, Università degli Studi di Torino, via P. Giuria 7, IT-10125, Torino, Italy.

[2] Departament de Ciència de Materials i Química Física and Institut de Química Teòrica i Computacional (IQTCUB), Universitat de Barcelona, C/ Martí i Franquès 1, ES-08028, Barcelona, Spain.

[3] Institució Catalana de Recerca i Estudis Avançats (ICREA), ES-08010, Barcelona, Spain.

[§] Authors contributed equally to this work.

[*] Corresponding authors: s.bromley@ub.edu, piero.ugliengo@unito.it.

Abstract

Infrared (IR) spectroscopy is the main technique used to identify and characterize silicate dust grains in astronomical environments. From IR spectra, the degree of crystallinity can be estimated and used to help understand the processing of dust occurring in different astronomical environments such as the interstellar medium (ISM) and circumstellar shells. Narrow spectral line shapes are assigned to crystalline grains, while broad signals are usually assumed to originate from amorphous material. Herein, we accurately calculate the IR spectra and energetic stabilities of several amorphous and crystalline silicate nanograins with an astronomically common Mg-rich olivinic (Mg_2SiO_4) stoichiometry and with sizes ranging from hundreds to thousands of atoms. Firstly, unlike at larger length scales, crystalline forsterite-like grains at the nanoscale, are found to be energetically metastable with respect to amorphous grains. However, from our careful analysis, we further show that the IR spectra of such nanosilicate grains cannot be unambiguously used to identify their structural nature. In particular, our work indicates that amorphous and crystalline silicate nanograins both exhibit broad IR spectra typical of non-crystalline grains, raising potential issues for estimates of the fraction of crystalline silicate dust in the ISM.

1. INTRODUCTION

Silicates are a fundamental constituent the of solid matter in the universe and are abundantly and ubiquitously detected as dust particles in several environments, *e.g.*, dense molecular clouds (MCs), circumstellar shells (CS) of young and old stars, comets and the interstellar medium (ISM).[1–5] The lifecycle of silicate dust is very complex and involves newly generated dust in the CS of old dying stars, destruction, regeneration and processing in the ISM and subsequent incorporation in MCs and protoplanetary disks.[1,2] Silicate dust is affected to a greater or lesser degree by the astrophysical conditions encountered throughout its journey. Knowledge of the structure and crystallinity of silicate dust can thus provide a diagnostic tool to help understand the physical and chemical conditions in a range of astronomical environments.

Infrared (IR) spectra provide the primary source of information regarding the atomistic structure of astronomical silicate dust grains. Observations where well-defined IR peaks can be discerned give strong support for the presence of highly crystalline grains (*e.g.*, in some CSs).[6] In such cases, comparison with laboratory IR spectra from carefully prepared samples can help deducing the crystal structures and chemical compositions of the observed dust grain populations. From such studies, it has been confirmed that crystalline silicate dust is very magnesium-rich and primarily of either pyroxene ($MgSiO_3$) and/or olivine (Ol, Mg_2SiO_4) composition.[7,8] IR spectra from the ISM are dominated by two broad peaks at around 10 and 18 μm that are attributed to silicate vibrational Si-O bond stretching and O-Si-O bond bending modes, respectively. Such spectra are usually interpreted as originating from amorphous silicates.[1] This assignment is supported by noting the strong similarity of such observed IR spectra with those from experimentally prepared bulk amorphous silicates.[9–12] Spectral analyses of carefully prepared laboratory samples have revealed that the position and width of these two characteristic IR peaks of dense glassy amorphous silicates vary, to an extent, with respect to the chemical composition,[1,9] and the degree of thermal annealing.[9–11] Interestingly, it has also been shown that experiments irradiating crystalline silicates with high energy ions, thus mirroring the environment of the ISM, can induce atomic disorder and porosity.[13] Although these irradiated samples spectroscopically appear to be very similar to dense amorphous silicates, they likely retain residual pockets of the original crystal order. By fitting observed IR spectra using various combinations of laboratory spectra, a number of investigations have attempted to gain insights into the properties and structure of amorphous silicate dust from the positions and shapes of the 10 and 18 μm silicate features.[11,14,15] Since the lifecycle of silicate dust involves different types and degrees of energetic processing, insights into the evolutionary history of grain populations and how processed they are can be gained from knowing their crystallinity. By fitting the observed 10 μm absorption

feature using laboratory IR spectra from both amorphous and crystalline silicate samples, an upper bound on the fraction of crystalline silicate in the ISM of 2.2% by mass was derived,[16,17] consistent with other more recent measurements.[18] Although such studies clearly point to a strong lack of crystalline dust grains in the diffuse ISM, we explore the possibility that observational IR spectra from putative amorphous grain populations could have contributions from a population of *quasi-crystalline* nanosized silicate grains.

In this work, we developed atomistic models of nanoparticles (NPs) with diameters varying between ~1.2 and ~4.6 nm and with a pure Mg_2SiO_4 olivinic composition. It has been estimated that such small NP grains could form up to 10% of the mass of the silicates in the ISM without violating observational constraints and, if so, could form the largest population of ISM silicate dust grains by number.[19] Indirect support for the existence of such a population of nanosilicate grains also comes from their potential role in explaining the anomalous microwave emission (AME) in the ISM.[20–22] We employ both quantum (QM) and classical (CM) mechanics calculations to model our nanograins with varying degrees of crystallinity and provide a detailed analysis of their structure and relative energetic stabilities. Our main focus is on how the crystallinity of such nanograins is reflected in their IR spectra. In order to assess this, we derive reliable IR spectra directly from accurately modelling the vibrational modes in our atomistically detailed silicate NP structures. Through this approach, we explicitly show that, unlike for larger grains, IR spectra do not provide a clear measure of crystallinity for nanograins. The possible implications of our results for estimating the crystallinity of astronomical silicate dust are discussed.

2. COMPUTATIONAL DETAILS

For all QM calculations, we used the CRYSTAL package,[23] while for CM calculations we used the GULP[24] and LAMMPS[25] codes.

2.1. Relative energies

For all calculations, the relative energies *per* Mg_2SiO_4 formula-unit with respect to bulk crystalline forsterite of our Ol NPs, ΔE^*, have been computed according to Eq. **1**

$$\Delta E^* = \frac{1}{N} E_{NP} - \frac{1}{4} E_{bulk} \qquad\qquad \mathbf{1}$$

where E_{NP} is the energy of an Ol NP with N formula-units, and E_{bulk} is the energy corresponding to a unit cell of crystalline forsterite containing 4 Mg_2SiO_4 units.

2.2. QM calculations

For the QM modelling, we used the CRYSTAL package, which can perform *ab initio* density functional theory (DFT) and Hartree-Fock calculations of periodic (*e.g.*, crystals, surfaces, polymers) as well as non-periodic (*e.g.*, molecules, NPs) systems. The wavefunction is expressed as a linear superposition of crystalline/molecular orbitals which in turn are expanded as linear superpositions of Gaussian-type functions centred on all atoms and constituting the *basis set*. All calculations were performed within the DFT framework, using the Perdew-Burke-Ernzerhof (PBE) functional,[26] and a specific basis set consisting of the following contraction: $(8s)$-$(61sp)$, $(6s)$-$(6211sp)$-$(1d)$ and $(6s)$-$(31sp)$-$(1d)$ for the Mg, Si and O atoms, respectively. In the following, we will refer at this basis set as "OIBS". A detailed description of the OIBS is provided in the Supporting Information (SI) file available online.

Default thresholds parameters were adopted for all energy calculations, geometry optimizations and IR frequency and intensity calculations. To evaluate the electron density, we used a pruned (75, 974) grid, consisting of 75 radial points and a maximum number of 974 angular points. At these points, Coulomb and exchange integrals were computed. All other technical details regarding these DFT calculations are reported in the SI.

2.3. CM calculations

We used the CM-based GULP code to perform the preliminary optimizations of bulk cut NPs, to amorphize the PBE-optimized NPs through molecular dynamic (MD) simulations, and to simulate IR spectra for all NPs. Specifically, for some preliminary optimizations, we used the general Reax force-field (FF),[27] while for all other GULP calculations we used the FF used by Walker *et al.*,[28] which is based on previously reported FFs developed by Price *et al.*[29] and Catlow *et al.*[30] All the parameters controlling the numerical accuracy of the GULP calculations were kept constant to default values. For geometric optimizations, we used either the standard Broyden-Fletcher-Goldfarb-Shanno (BFGS) algorithm or, when necessary, the Rational Function Optimization (RFO) algorithm.[31,32] IR intensities were computed from the Born effective charge tensor.[33] All MD simulations used in the amorphization of bulk cut NPs were performed at either 1800 or 2400 K within the canonical ensemble (NVT) using a 1 fs timestep and with initial velocities randomly generated at 800 K.

For preparing the nucleated NPs, we used MD-based simulations using the CM-based LAMMPS code (see Subsection 3.1.3 below). Here we progressively built NPs by addition of monomeric species (SiO, O and Mg) following the heteromolecular homogeneous nucleation route proposed by Goumans & Bromley.[34] Each monomeric addition step was performed within the microcanonical ensemble

(NVE) with a timestep of 0.5 fs and using the Berendsen thermostat to maintain the temperature between 1000-800 K, typical for dust nucleation CS environments.

We checked the reliability of the PBE/OlBs and Walker FF methodologies by comparing the simulated structural (lattice parameters) and spectroscopic IR features of crystalline forsterite with those from experimental measures. **Figure 1** shows the comparison of IR spectra (the experimental spectrum from a sample of amorphous Mg_2SiO_4 olivine material is also included) while **Table S2** of the SI file shows the structural details in terms of the forsterite cell parameters. Experimental spectra are taken from a recent work and reproduced with the authors' permission.[35] Structural data are in excellent agreement with the experimental ones (errors are within ~1%, **Table S2**) for both CM and QM based methodologies. The simulated spectra are generally in good agreement with the experimental IR spectrum for forsterite. In particular, both the QM-based (PBE/OlBS) and the CM-based (Walker FF) show two distinct Si-O stretching peaks between 10-12 µm with similar relative intensities as in the experimental spectrum. Also, both simulated spectra exhibit a characteristic feature at ~22-23 µm. The PBE/OlBS spectrum also shows peaks between 16 and 19 µm in agreement with the experimental spectrum. These peaks are not so evident in the Walker FF spectrum, indicating that this CM-based method may find it more difficult to reproduce O-Si-O bending modes. For the purpose of the present work, we are predominantly interested in the relative amount of discernible detail in the IR spectra for our different sets of Ol NPs. As such, the two methods we employed are clearly able to provide well-defined IR spectra with narrow characteristic peaks of crystalline material, and this is sufficient for our purposes.
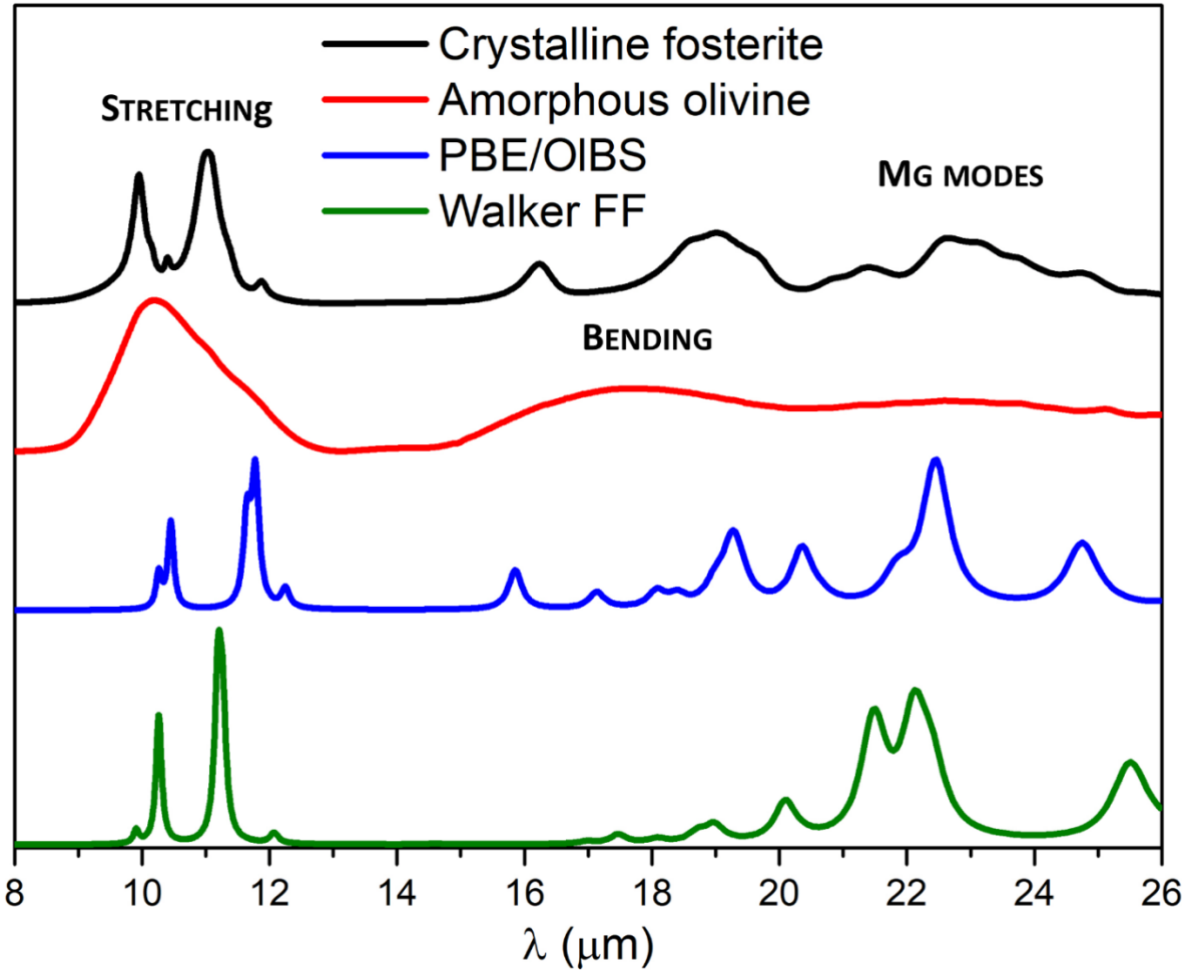
Figure 1 Experimental spectra (from Ref. 35) for crystalline forsterite (in black) and amorphous Mg_2SiO_4 olivine (in red) compared with calculated IR spectra using CRYSTAL at PBE/OlBS level (in blue) and GULP with the Walker FF (green). Intensity is in arbitrary units and spectra are vertically shifted for ease of comparison.

3. RESULTS AND DISCUSSION

In this Section, we explain the procedures we followed to generate our different NP models (Subsection 3.1), then we present and analyse the results from an energetic and structural point of view (Subsection 3.2) and, finally, we show and discuss the simulated IR spectra of the NPs (Subsection 3.3). **Figure 2** schematically summarises the methods we followed to produce our atomistic NP models, the calculations performed within this work, and the methods used to define the initial geometries of our Ol NPs. **Figure 3**, **4**, **5**, and **6** show the initial and PBE/OlBS-optimized structures of some selected NPs.
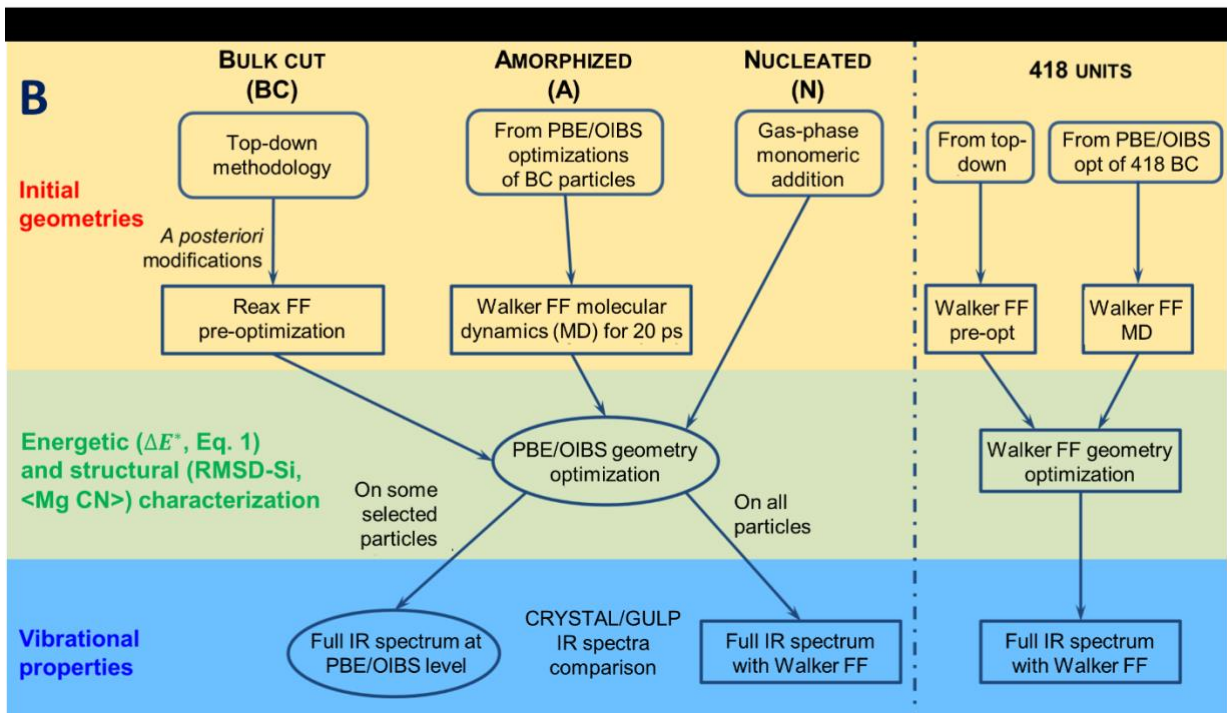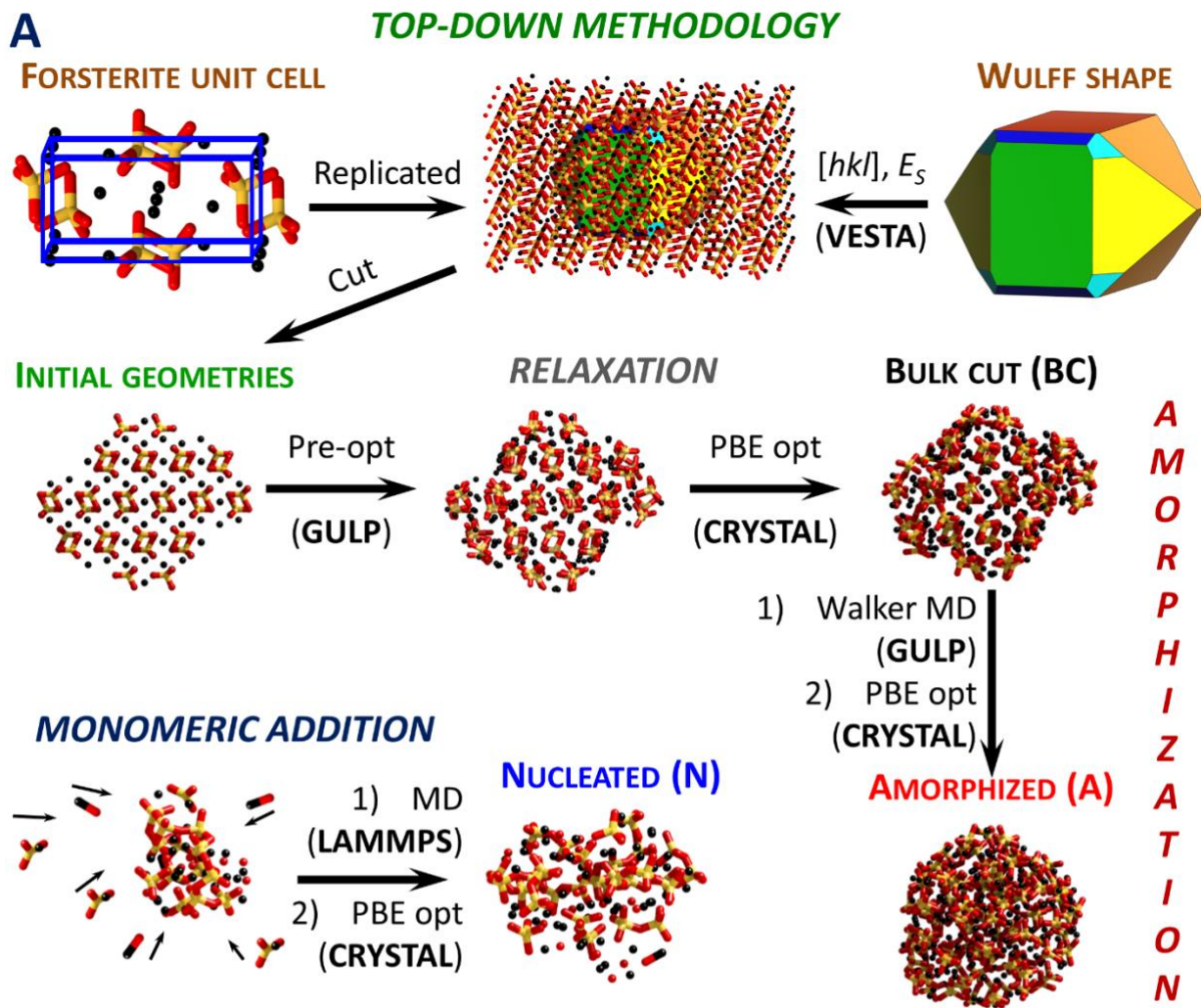
Figure 2 A: graphical representation of the procedures followed to obtain our three types of Ol NPs. *i*) bulk cut – BC – NPs (top-down methodology, followed by structural relaxation using the GULP

code at Reax FF level), *ii*) amorphized – A – NPs (MD-based amorphization at high temperatures using the GULP code with the Walker FF), and *iii*) nucleated – N – NPs (from gas-phase monomeric addition). Atom colour code: Si - yellow, O - red, Mg - black. **B**: schematic representation of the methods employed in the work. In rounded rectangles we outline the methods we used to define the initial geometries of our NPs (**Figure 2 A**). Square rectangles represent FF calculations (GULP) while ellipses represent PBE/OlBS calculations (CRYSTAL). The scheme on the right-hand side of the straight dot-dashed line refers only to the 418 formula-units NP, for which slight modifications of the NP-generation procedure were necessary (see Sections 3.1.1 and 3.1.2) and for which all properties were calculated exclusively with FFs.

3.1.   Generation of NPs

To simulate Ol NPs, we developed three different sets of NP models, namely *bulk cut* (BC) or *crystalline*, *amorphized* (A) and *nucleated* (N) NPs. Hereafter we label our NPs as "*Ny Z*" where *N* represents the number of formula-units, Z = BC, A or N (*i.e.*, it indicates the set which the NP belongs to) and *y* can be any additional information necessary to identify the NP in question.

3.1.1.   *Bulk cut (BC) crystalline NPs*

Bulk cut NPs have been generated following the top-down methodology, starting from the Wulff construction (*i.e.* following the shape of a macroscopic, perfect crystal, **Figure 2**, panel **A**, top-right corner) of forsterite. We note that this method has already been successfully used to model NPs of binary oxide systems such as titania and ceria.[36,37]

The main steps we followed in this top-down approach were:

–   using CRYSTAL, we firstly optimized the crystallographic structure of the forsterite unit cell using DFT calculations at a PBE/OlBS level of theory (top-left corner of panel **A** of **Figure 2**);[38]

–   using the VESTA software,[39] we replicated the unit cell several times and then cut along the crystallographic directions representing the most energetically stable surfaces of forsterite crystals,[40] as derived from previous DFT calculations.[41] During this phase, the initial choice of the unit cell origin can play a fundamental role in the final shape and stability of the resulting NP, thus we also studied bulk cuts after translating the forsterite unit cell. NPs generated after this translation have been labelled with "trasl". For more details, see the SI.

The NPs generated after this top-down method represent our initial set (**Figure 3**). After some *a posteriori* structural modification, and pre-optimization using Reax FF, we finally fully optimized the NPs at a PBE/OlBS level of theory (see resulting structures in **Figure 4**). All the details concerning the top-down procedure, the *a posteriori* NP modifications and the Reax FF optimisations are reported in the SI. For the largest BC NP studied in this work (418 formula-units), as the PBE/OlBS

optimization was very computationally-demanding, we only employed CM-based calculations. All reported energetic and structural results concerning this NP refer to the calculations using the Walker FF (right-hand side of **Figure 2 B**). For the details, please see the SI.

3.1.2.   *Amorphized (A) NPs*

Using the GULP code, BC PBE/OlBS-optimized NPs were heated using classical MD simulations at 1800 K with the aim of amorphizing their structures. For one NP only (30a BC), we also tested a higher temperature of 2400 K, to check for temperature effects on the final structure and morphology of the NP (see Sections 3.2 and 3.3 for details). For most NPs, after a 10 ps equilibration, we ran MD simulations for 20 ps of production time. For the largest 418 formula-units NP, a significantly longer 200 ps production time was found to be necessary to amorphize the NP. Further details about these MD runs are available in the SI. These amorphized particles were then optimised at PBE/OlBS level of theory using CRYSTAL (see **Figure 2**, panel **B**). The final optimized NP structures are shown in **Figure 5**.

3.1.3.   *Nucleated (N) NPs*

Since the A NPs were generated by thermal annealing of BC NPs, it is possible that they can still retain geometric similarities with the original crystalline structures. As silicates in the ISM may form by condensation from the gas-phase under non-equilibrium conditions, amorphous silicate grains, however, can be completely unrelated to bulk crystal structures. Therefore, we also constructed NPs using a bottom-up procedure through monomeric addition ensuring no relationship with the forsterite crystal structure and then ran MD at 1800 K simulations using the LAMMPS code. These N NPs were then finally optimised at PBE/OlBS level of theory using CRYSTAL (see resulting NP structures in **Figure 6**).

It is worth noting that, as a consequence of the way they are generated, these N NPs often appear to display as a solid solution of MgO, pyroxenes (-Si-O- chains) and pure olivine, although their stoichiometries are the same as that of pure forsterite. This differentiation of phases is particularly evident for the smaller NPs (see, for example, the 30 N NP of **Figure 6**) where the structures are quite distinct to that of forsterite (the forsterite unit cell structure is reported in top top-left corner of **Figure 2**, panel **A**).
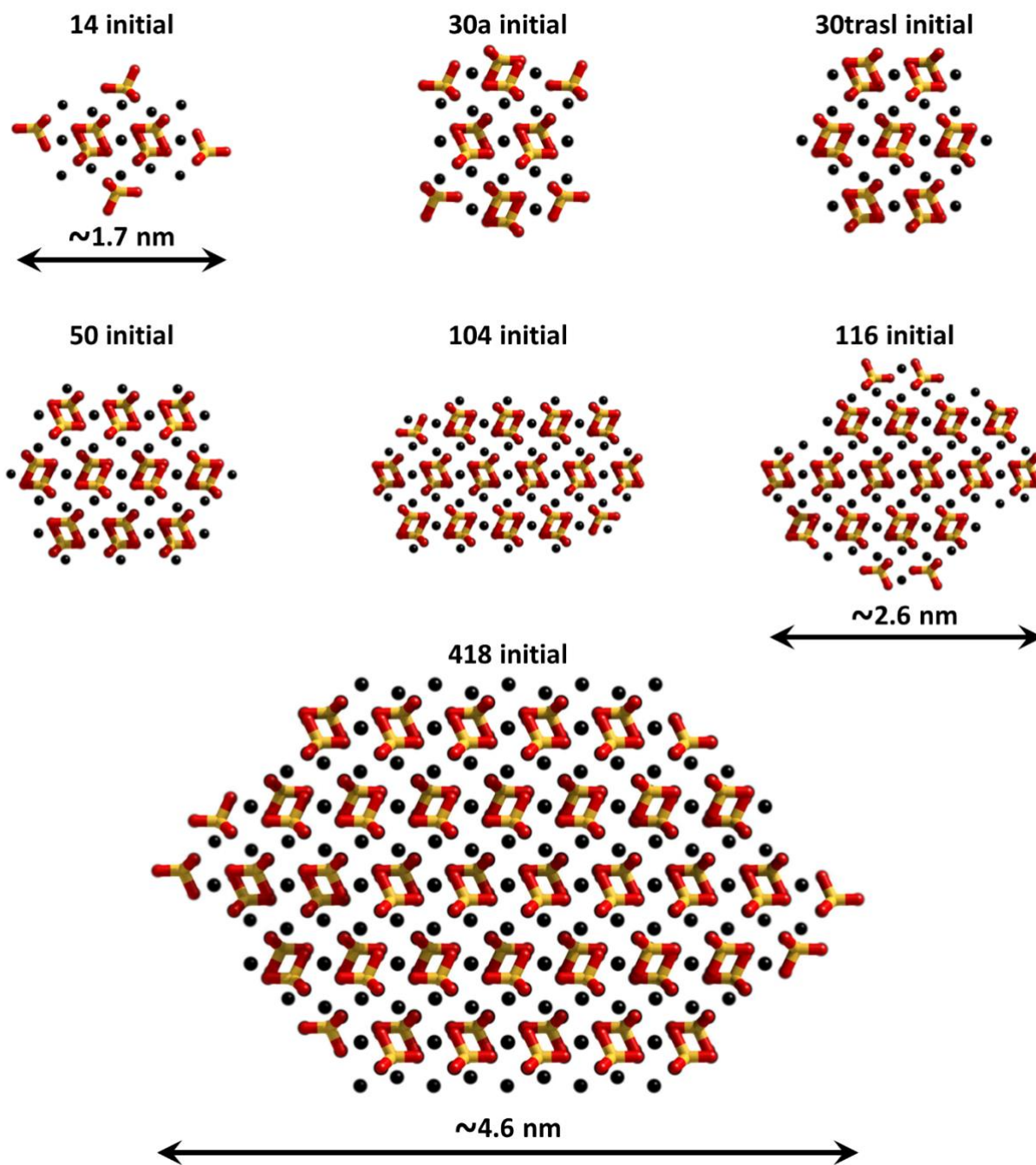
Figure 3 Selected structures of the set of initial unrelaxed Ol NPs (see Subsection 3.1.1), *i.e.* with structures frozen to those of the original forsterite crystal. Colour code: same as **Figure 2**. Note that the relative NP sizes are not to scale. See **Figure S1** of the SI for the full set of initially NP structures.
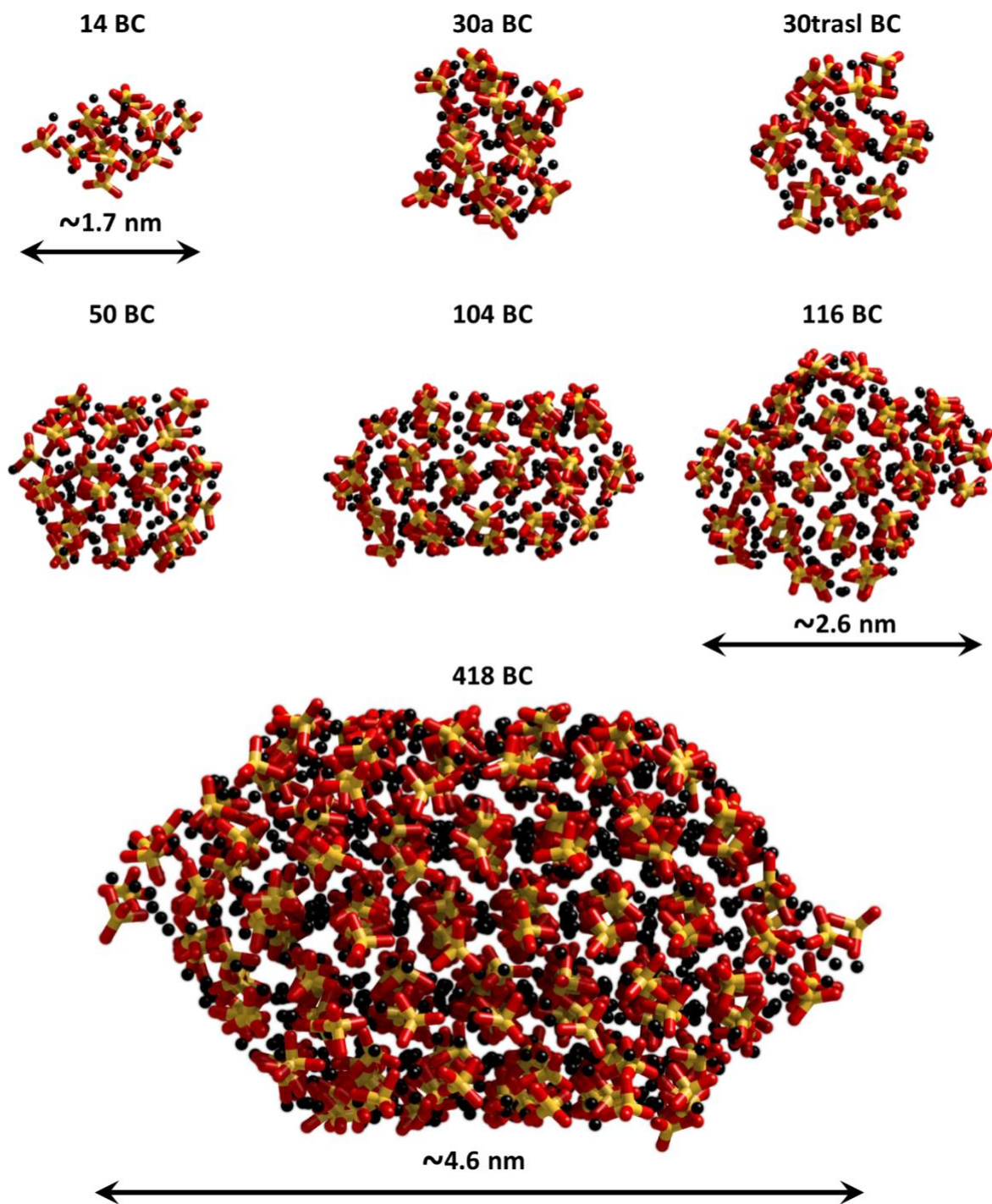
Figure 4 Selected structures of the set of optimised PBE/OlBS bulk cut (BC) NPs particles (Subsection 3.1.1), *i.e.* NPs resulting from energy-lowering relaxation of the NP structures in **Figure 3**. Colour code: same as **Figure 2**. Note that the relative NP sizes are not to scale. See **Figure S2** of the SI for the full set of BC NPs.
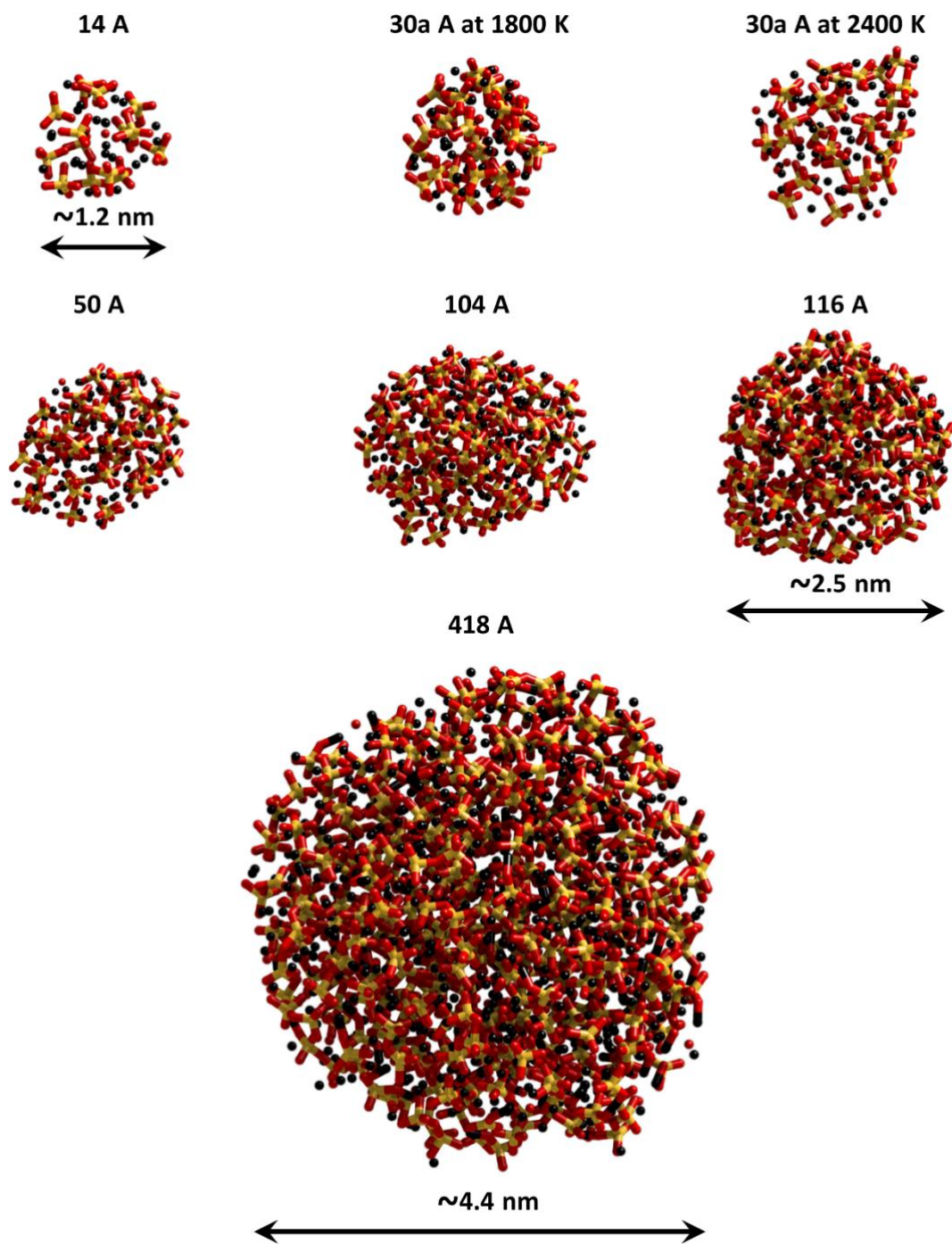
Figure 5 Selected structures of the set of amorphized (A) NPs, after PBE/OlBS optimization (Subsection 3.1.2). Colour code: same as **Figure 2**. Note that the relative NP sizes are not to scale. See **Figure S3** of the SI for the full set of A NPs.

Figure 6 Selected structures of the set of nucleated (N) NPs, after PBE/OlBS optimization (Subsection 3.1.3). Colour code: same as **Figure 2**. Note that the relative NP sizes are not to scale. See **Figure S4** of the SI for the full set of N NPs.
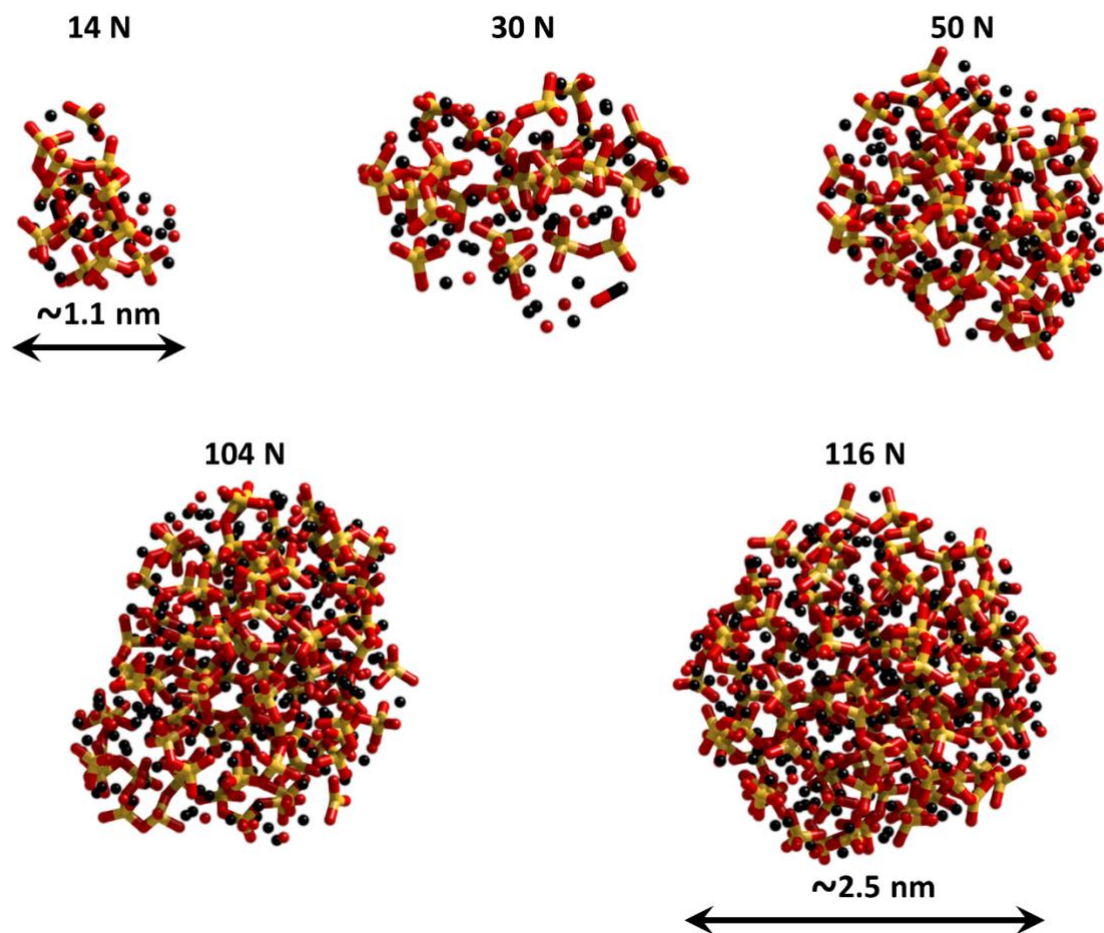
3.2.   Energetic and structural features

3.2.1.   *Energetics and stability*

The relative energetic stability of our PBE/OlBS-optimized NPs per Mg_2SiO_4 formula-unit with respect to the forsterite bulk (ΔE^*) has been computed according to Eq. **1**. ΔE^* values (in kJ mol$_{-1}$) for all NPs are reported in **Table 1**, together with other structural properties. We have grouped the data with respect to the number of formula-units N in order to facilitate a comparison between NP models of the same size. The NPs containing 30 formula-units are used as a test case to show the effect of different methods to generate the crystal cuts as well as different annealing temperatures. 30a BC and 30b BC NPs correspond to two different crystalline cuts for the 30 formula-units non-translated NP (**Figure 3** and **Figure 4**). The 30a A at 1800 K and 30a A at 2400 K NPs have been amorphized using two MD runs at 1800 and 2400 K, respectively (**Figure 5**).

13

The overall energetic stability is clearly affected by the different processes involved in the generation of a given NP which highlights the importance of carefully generating such NPs in order to estimate the amorphous *vs* crystalline stability cross-over size regime. For example, the difference in energy *per* formula-unit between the 30a BC and 30trasl BC NPs is 23.6 kJ mol–1 (**Table 1**). This energy difference is close to that between forsterite and the energetically metastable wadsleyite Mg_2SiO_4 crystal polymorph (~32 kJ mol–1).[42] This result highlights the importance of generating top-down BC NPs from unit cells with different translated origins. Generally, this can also be seen from the fact that the lowest lying BC NP structure (highlighted in bold in **Table 1**) is neither consistently in the translated ("trasl") nor in the non-translated series. Conversely, different amorphization temperatures (1800 *vs* 2400 K) do not appear to significantly affect the final results, at least from an energetic stability (ΔE^*) point of view.

Table 1 Summary of energetic and structural data for all PBE/OlBS-optimized olivinic NPs. n is number of atoms, N the number of Mg_2SiO_4 formula units. Relative energies with respect to forsterite bulk (ΔE^*, Eq. **1**) are in kJ mol–1 *per* formula-unit. <Mg CN> values correspond to the overall average coordination numbers of Mg ions. Root-mean-square-displacements of the silicon atoms (RMSD-Si) are given in Å. ΔE^* values for the most stable bulk cut and amorphized NP for each N are highlighted in bold.

NP model	n	N	$N^{-1/3}$	ΔE^*	<Mg CN>	RMSD-Si
14 BC	98	14	0.415	**420.1**	4.25	1.12
14 A				**382.0**	4.14	3.95
14 N				474.2	4.04	-
30a BC	210	30	0.322	357.9	4.35	0.95
30b BC				346.4	4.48	1.05
30trasl BC				**334.3**	4.55	0.90
30a A at 1800 K				331.1	4.37	3.24
30a A at 2400 K				340.5	4.30	6.44
30trasl A				**327.0**	4.50	3.40
30 N				417.5	4.18	-
50 BC	350	50	0.271	**298.7**	4.64	0.78
50trasl BC				311.5	4.61	0.98
50 A				282.0	4.56	2.86
50trasl A				**280.2**	4.64	2.04
50 N				350.7	4.31	-
60 BC	420	60	0.255	304.3	4.53	1.09
60trasl BC				**301.0**	4.55	0.85
60 A				281.6	4.56	3.32
60trasl A				**273.6**	4.54	1.70

60 N				350.1	4.43	-
80 BC	560	80	0.232	**287.0**	4.71	1.04
80trasl BC				294.2	4.68	0.73
80 A				272.4	4.61	3.72
80trasl A				**255.4**	4.65	2.26
80 N				323.4	4.38	-
92 BC	644	92	0.222	**263.3**	4.72	0.67
92trasl BC				281.5	4.71	0.77
92 A				264.9	4.58	3.45
92trasl A				**246.8**	4.65	2.15
92 N				329.3	4.39	-
104 BC	728	104	0.213	267.4	4.78	0.55
104trasl BC				**259.9**	4.72	0.64
104 A				262.7	4.53	2.94
104trasl A				**249.0**	4.67	2.18
104 N				318.5	4.45	-
116 BC	812	116	0.205	**255.9**	4.84	0.83
116trasl BC				272.2	4.71	0.94
116 A				250.6	4.63	3.04
116trasl A				**235.5**	4.69	2.15
116 N				308.3	4.49	-
418 BC*	2926	418	0.13	**82.9**	5.04	0.97
418 A*				**86.0**	4.74	9.21

*: data from Walker FF-optimizations only (see **Figure 2**, panel **B**, right-hand side).

Figure 7 provides the ΔE^* values as a function of $N^{-1/3}$, following the spherical cluster approximation (SCA) that relates the energy of a NP with the ratio between its surface and bulk atoms.[43] We note that the SCA is only a first order geometric approximation that does not take into account the atom/electronic degrees of freedom (*e.g.*, surface stress) in realistic NPs, which roughly correspond to higher order terms.[36] We find that the lowest energy structures of each family of crystalline, amorphous and nucleated NPs follow well a simple fitted $N^{-1/3}$ dependence, with R[2] values of 0.982, 0.986 and 0.979, respectively. Hence, even if some of the NP structures do not correspond to the lowest energy minima for that family of NPs, these simple fits can provide a tentative estimate of the size dependent energetic trends for each of the NP families.
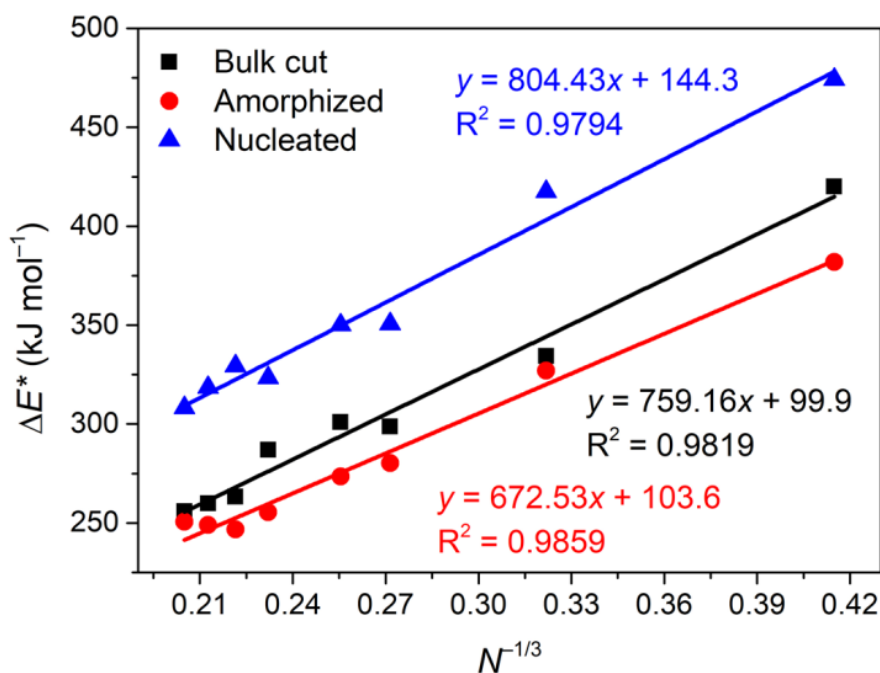
Figure 7 Relative energies with respect to forsterite bulk *per* formula-unit (ΔE^*) for the most stable NPs we found for each size, as a function of the number of formula-units (N): the linear correlation fitting parameters and R_2 values are also reported close to each respective line.

We first note that the A NPs are the most energetically stable NPs for all considered sizes. Although A NPs are always more stable that N and BC NPs, we note that the largest A NPs of 104 and 116 formula-units are higher in energy *per* unit than the smaller 92 unit A NP. This result clearly indicates that the 104 and 116 A NP models are not the most stable amorphous NPs for their size. As found in other NPs systems,[36] the BC NP structures are more energetically unstable relative to the A NPs for the smallest sizes, but converge faster to the bulk limit (*i.e.*, the fitting line for BC NPs has a steeper slope than that for A NPs), as expected by the fact that crystalline forsterite is the most stable bulk phase of the Mg-rich olivine family. This implies that any process which generates small crystalline NPs will be generating metastable particles which will, upon annealing, evolve towards amorphous structures. Although the exact energy evolution for each family is not precise due to the use of the SCA and the fact that not all NPs are the lowest energy for their type and size, we can extrapolate the fitted lines to roughly estimate the energetic cross-over point between amorphous and crystalline NPs. Following a previous study,[44] we convert the number of formula-units to the radius of a NP assuming a spherical shape and a volume *per* Mg_2SiO_4 unit extracted from bulk forsterite. With the current available data, the cross-over between A and BC NPs appears to occur at a diameter of ~12 nm, which is quite far away from the NP sizes explored within this work. Finally, the N NPs appear to be the most energetically unfavourable species, typically being ~50 kJ mol$_{-1}$ less stable than the BC NPs. It is reasonable to suggest that the large metastability of N NPs arises from their "glass-like" silicate

disorder and the sub-optimal mixing of MgO units into their structure. There is still an ongoing debate on the formation mechanisms of silicate dust in the envelopes of asymptotic giant branch (AGB) stars. Observational evidence seems to show the preferential formation of amorphous material with respect to crystalline NPs,[45] while thermodynamics based on extended systems always assume the formation of the most stable bulk phase, which is crystalline Ol.[46] The results in this work highlight the necessity to consider the formation of amorphous Ol NPs as a possible route for the condensation of silicate species in CS, probably aiding to bridge the discrepancy between purely thermodynamic arguments and observational evidence. It must also be considered that, although on thermodynamics grounds, the smallest silicate grains should be amorphous, the actual structure of dust particles of such dimension in CSs and the ISM will not depend only on the energetics, but also on several processes like accretion from nucleation centres, temperature-related kinetics effects, high- and low-energy collisional events involving cosmic rays and/or other dust particles.[1,2,6,47,48]

3.2.2. *Structural descriptors and characterization*

The energetic analysis performed in Subsection 3.2.1 suggests the existence of at least three energetically-distinguishable phases of small Ol NPs: amorphous material with mainly isolated $[SiO_4]^{4-}$ tetrahedra, crystalline forsterite, and glass-like NPs with some segregated pockets of MgO and more polymerised $[SiO_4]^{2-}$ units. From an energetic point of view, these three phases are represented by our three sets of A, BC and N NPs, respectively. Experimental characterization of these phases at such a small scale would be extremely challenging. Theoretically, however, with direct access to the detailed atomistic structure, we can begin to quantitatively analyse the structural differences among these three NP families.

Silicates are structurally complex inorganic materials due to the presence of both ionic (Mg-O) and semi-covalent (Si-O) bonds, with the former being weaker than the latter. The difference in bond energy causes Mg cations to be more mobile, while the SiO_4 anionic units are more rigid but can create complex polymerized networks with little energetic cost. In order to structurally characterize our NPs, we first take the crystalline forsterite phase as a crystalline benchmark which we describe in terms of tetrahedral units of SiO_4 that are regularly interspaced by octahedrally coordinated Mg cations. Secondly, we assume that the degree of crystallinity of NPs can be described by two structural measures which we take to be optimal in the Ol bulk crystal: *i*) short-range structural order, which is related to the orientation and distortion of SiO_4 tetrahedra and MgO_6 octahedra, at their fixed lattice sites, and *ii*) long range periodic order, which is related to the repeated presence of the SiO_4 and MgO_6 units along the crystal lattice vectors.[38,40] In this work, we use the average Mg-coordination number (<Mg CN>) and the structural of distortion SiO_4 tetrahedra to describe short range order and the root-

mean-square-displacement of silicon atoms (RMSD-Si) to describe long range order. The use of <Mg CN> as a short-range order descriptor is justified by the fact that reorientation of silicate tetrahedra and displacement of Mg cations from their equilibrium geometries will cause changes in the Mg-O distances and hence to the coordination numbers. It is reasonable to assume that amorphization using mild temperatures will involve small changes in the orientation and/or distortion of the different units, especially for the lower coordinated (*i.e.* least well bound) atoms at the surface. Surface relaxation of an NP can thus be seen as a local amorphization taking place at the outermost layers of the NP which should be reflected in the <Mg CN> values and the spatial distribution of SiO_4 structural distortion. On the other hand, a higher temperature amorphization should cause a strong displacement of the different SiO_4 units, with the possibility of inducing polymerization of the silicate skeleton. The displacement of the SiO_4 units can be analysed through the RMSD-Si. Although the RMSD-Si is a natural way in which to compute the displacement in the MD amorphized NPs with respect to the corresponding parent BC NP, the comparison with the nucleated NPs is not straightforward, as the atomic assignment cannot be unequivocally matched to an original crystalline structure. We therefore only provide RMSD-Si values for the A NPs in order to compare MD amorphized NP structures with the BC NPs.

In **Figure 8**, we show illustrative examples of crystalline (left), locally-amorphized (centre) and globally-amorphized (right) Ol structures. In the left panel, the perfect periodic structure of crystalline forsterite can be easily recognized, with the oxygen atoms of the isolated silicate tetrahedra coordinating to the Mg cations. In the centre panel, a mild amorphization has partially altered the original crystalline structure, but some crystalline features are evidently retained, while in the right panel, a higher temperature amorphization results in a structure lacking any clear remnants of crystallinity. Although the structures in the right and centre panels of **Figure 8** both represent amorphous Ol, both RMSD-Si and <Mg CN> structural descriptors can help us to analyse whether they have some intrinsic structural features that allow one to distinguish them in our NPs.
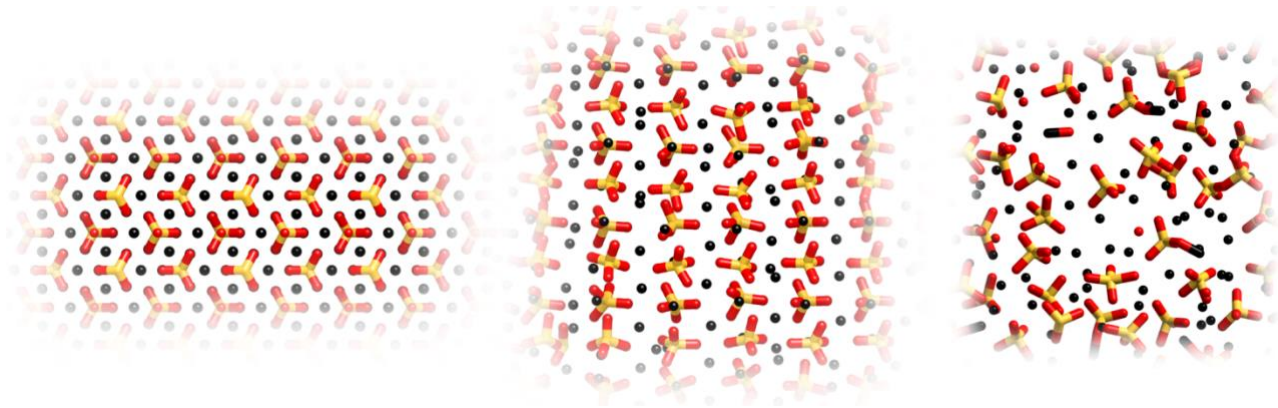
Figure 8 Left: periodic structure of perfectly crystalline forsterite. Centre: structure for a non-crystalline olivinic material, preserving a partial long-range order (Si and Mg atoms are disposes in "column and rows", but silicate tetrahedral are partially distorted and rotated). Right: structure for a non-crystalline bulk material with a forsterite stoichiometry with no local and periodic order (highly distorted and partially polymerised SiO_4 tetrahedra, with some formation of MgO units). Colour code: same as **Figure 2**.

In the left panel of **Figure 9** we graphically report the RMSD-Si data for all the PBE/OlBS-optimized NPs (data for the 418 formula-units NPs are omitted for a clearer representation. See **Table 1** for the values). The RMDS-Si values for BC particles are low even for the smallest considered NP sizes. For A NPs, the RMSD-Si values are several times larger and spread over a wider range. These data show that BC NPs preserve a high degree of periodic crystalline order, while the relatively lower crystallinity of the A NPs is clear.
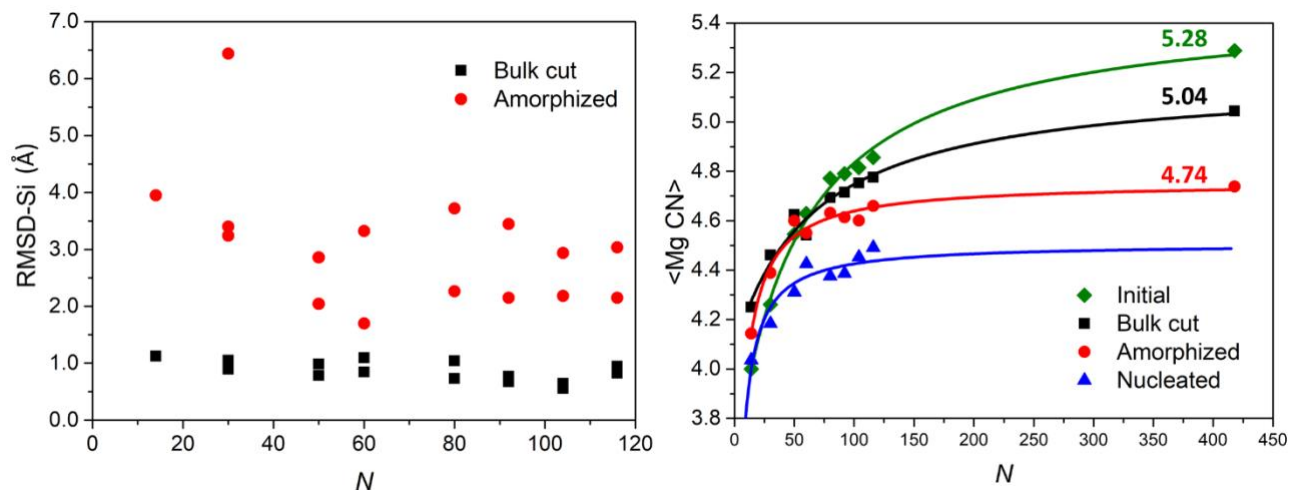

Figure 9 Left panel: Root-mean-square-displacements of the silicon atoms (RMSD-Si) in Å with respect to the initial cuts of **Figure 3** as a function of the size of the particles, N (data for the 418 formula-units NPs are not shown. See **Table 1** for the numerical values). Right panel: Average Mg coordination numbers, <Mg CN>, as a function of the size of the particles (N). See **Table 1** for the numerical values. The numerical values correspond to the largest 418 formula-units NPs. Lines are added as a guide to the eye.

Finally, we note that the RMSD-Si value for the 30a A NP after a 2400 K MD run is almost double that of the corresponding NP after a 1800 K MD run (3.24 Å *versus* 6.44 Å, **Table 1**), with the latter value being the highest among all PBE/OlBS optimized particles. This indicates that the use of higher temperatures could produce an even more amorphized NPs. However, as we will show in next Section, this large difference in the RMSD-Si value does not produce significant differences in the simulated IR spectra.

In the right panel of **Figure 9**, we graphically show the <Mg CN> values as a function of the number of formula-units N for our three sets of NPs, plotting the average when we have more than one NP for a given N. In this figure, the <Mg CN> values of the initial NPs (**Figure 3**) are also incorporated in order to compare the values with respect to the perfect crystalline structure for every NP size (see **Table 1** for values). From **Figure 9**, it can be seen that the initial unrelaxed cut NPs have the largest <Mg CN> values of all considered NPs, corresponding to the fact that, by construction, they are structurally most like the bulk crystal. However, even for this family of NPs, the largest initial cut NP has a <Mg CN> value of 5.28 which is still significantly different from the bulk crystal limiting value of 6 due to the lower coordination of Mg cations near the NP surface. From the other three families of NPs, as expected, BC NPs have <Mg CN> values which are the closest to those of the initial cut NPs. Here the largest BC has a lower <Mg CN> value of 5.04 indicating that initial cut NPs preferentially relax to lower energy structures with slightly lower crystallinities. The lowering of <Mg CN> values going from the perfect initial cut NPs to relaxed BC NP structures points to the fact that even the most crystalline material at the nanoscale cannot be described as completely crystalline. Visual inspection of the NPs suggests that the BC NPs should be considered as being core-shell structures (*i.e.*, with highly crystalline cores and slightly disordered near surface shells). For the largest A NP, the <Mg CN> value is equal to 4.74, while for a hypothetical 418 N NPs it can be predicted from the trends of the existing data to be even smaller (~4.60). These lower <Mg CN> values correspond to a higher degree of local structural disorder and thus even lower crystallinities. These data strengthen our above analysis concerning the structural (and energetic) distinguishability of BC, A and N NPs.

The <Mg CN> and RMSD-Si values are averages over the whole structure of a NP and thus do not spatially differentiate regions of more or less local structural change within a NP. Changes in both O-Si-O angle and Si-O bond distances are typical ways in which local structural relaxation can take place. Although separated in IR spectra, relaxations of these structural features combine to distort the $[SiO_4]^{4-}$ tetrahedra in NPs. From our discussion above, we should expect that the in a relaxed BC NP the relaxation of $[SiO_4]^{4-}$ tetrahedral should be mainly close to the surface, whereas for an amorphous

NP we should expect all $[SiO_4]^{4-}$ tetrahedral to be fairly equally distorted. In **Figure 10**, we show two cuts through the relaxed 116 BC NP (left) and a cut through the 116 A NP (right) showing only the Si atoms and where the degree of local $[SiO_4]^{4-}$ tetrahedral disorder (*i.e.* of the surrounding four oxygen atoms which are not shown) is related to the colour of the Si atom in question. We take the tetrahedral arrangement of oxygen atoms around the Si atoms in forsterite as our benchmark for the highest tetrahedrality. We measure the degree of distortion of each $[SiO_4]^{4-}$ centres by taking the RMSD of the atom positions with those of rotationally aligned $[SiO_4]^{4-}$ centre from the forsterite crystal. In **Figure 10**, we give the lightest colour to Si atoms with associated $[SiO_4]^{4-}$ centres having structures very close to those in forsterite and progressively darker shading to more distorted tetrahedrons. For the amorphized 116 formula-unit NP (right, **Figure 10**) the darker shading of all Si atoms shows that all $[SiO_4]^{4-}$ centres have significantly distorted structures. However, for the BC (left, **Figure 10**) it is clear that significant tetrahedral distortion only occurs at the surface of the NP (*i.e.* due to surface relaxation).
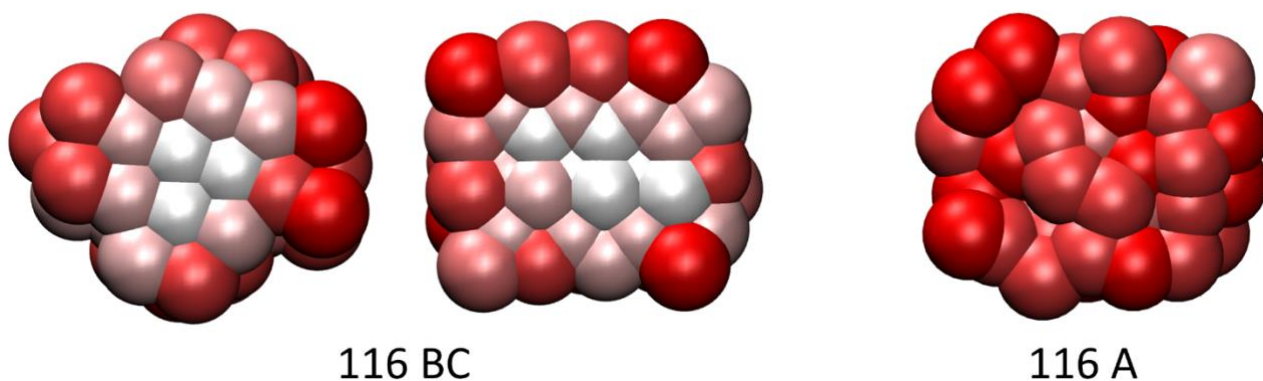

Figure 10 Cuts through 116 NPs showing only Si atoms with the degree of local tetrahedral distortion of the associated $[SiO_4]^{4-}$ centers indicated by shading (lighter: less distortion; darker: more distortion). Left: two perpendicular cuts through the 116 BC NP. Right: a single cut through the 116 A NP.

In summary, from our average measures (*i.e.* <Mg CN> and RMSD-Si values) we find that BC NPs preserve a higher degree of periodic crystallinity than A NPs, while BC, A and N NPs all show some degree of local structural distortion which increases with the level of amorphization. We note that our BC NP structures correspond to the most crystalline possible morphologies for their size (*i.e.* relaxed crystal cuts), even though our structural measures show that they do not possess the full structural order of the perfect, infinite crystal. In principle, average local structural measures such as our <Mg CN> values could be measured and/or observed from X-ray absorption spectra. Interestingly, preliminary estimates of the proportion of crystalline dust in the ISM based on such X-ray observations have placed tentative upper limits which are significantly in excess of those derived

from IR observations.[49] From our spatially resolved maps of tetrahedral distortion of individual $[SiO_4]^{4-}$ centres, we can further confirm that, although amorphized NPs are distorted fairly homogeneously throughout their structure, the main contribution to local structural disorder in BC NPs is through surface relaxation.

3.3. Full IR spectra

3.3.1. Simulated full IR spectra

Besides structural identification, it is important to establish whether our Ol NPs can be characterized by IR spectroscopy, as this corresponds to the main astronomical observable for silicate dust grains. Consequently, we employed frequency calculations to obtain the full IR spectra of all optimized NPs. All IR spectra, calculated using GULP for the larger NPs, and CRYSTAL for the smaller NPs, as well as the comparisons between the two, are reported in the SI.

The PBE/OlBs full IR harmonic spectra with CRYSTAL were simulated only for a few NPs, *i.e.*, all the 14 and 30 formula-units NPs and the 50 BC NP. For all NPs, we also simulated the full IR spectra with the GULP code at the Walker FF level (**Figure 2**, panel **B**). In all cases the line shapes of the IR spectral peaks were obtained from sums of Gaussian functions centred at the computed IR frequencies with heights adjusted to the corresponding absolute IR intensities. The full width at half maximum (FWHM) for the Gaussian functions was set equal to 10 cm$_{-1}$. This choice is justified below (see Subsection 3.3.2). In **Figure 11**, **A**-**E** panels, we report the full IR spectra for some selected particles in the 8-26 μm (1250-385 cm$_{-1}$) region. See **Figure 4**, **Figure 5** and **Figure 6** for the corresponding structures. The full set of IR frequencies and intensities for all NPs computed with either CRYSTAL or GULP are available online in a separate file for each NP. The reliability of the IR spectra from both CRYSTAL and GULP calculations is confirmed through a comparison with experimental data for both amorphous and crystalline Ol (**Figure 1**).
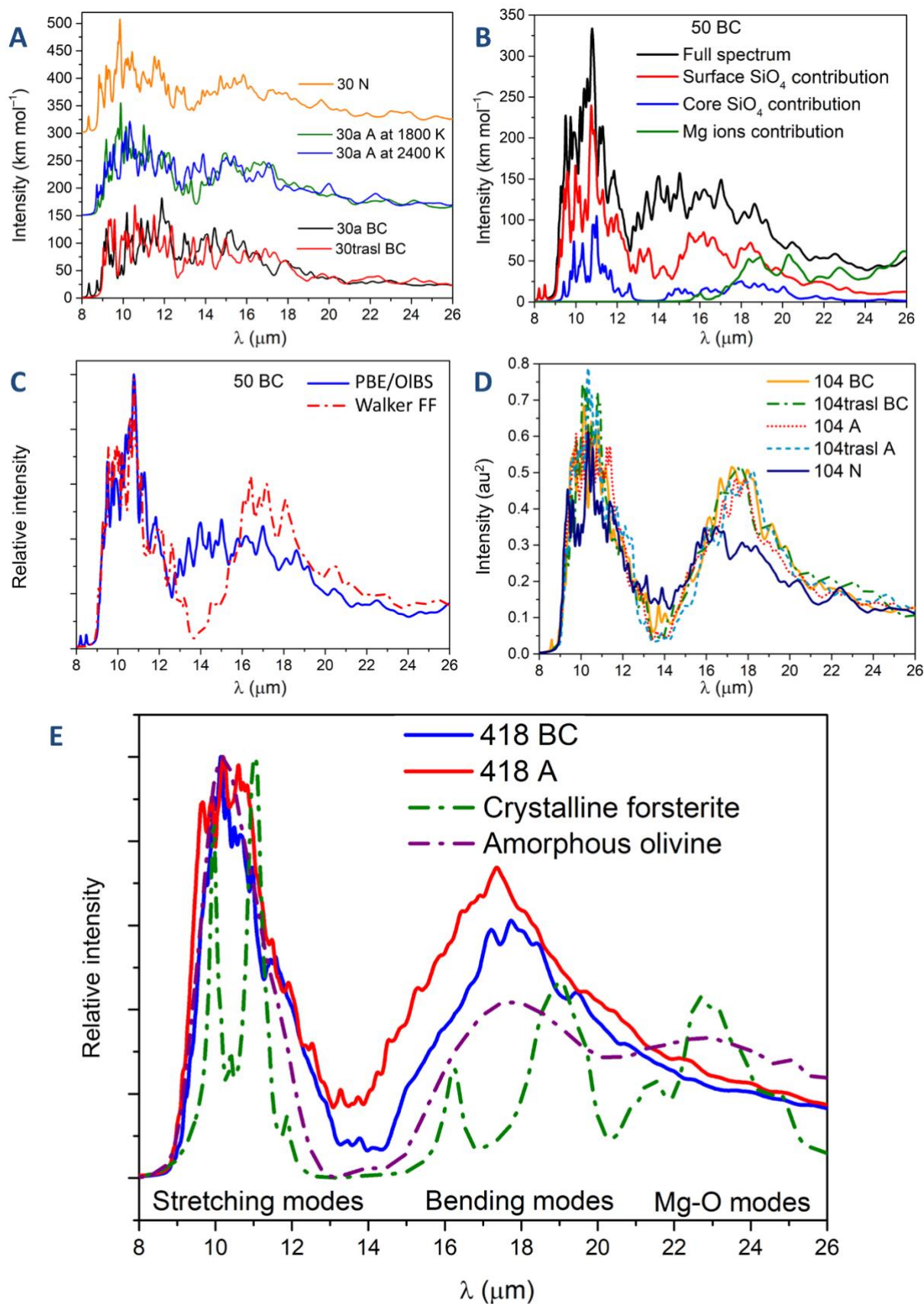
Figure 11 A-E: Simulated IR spectra for some selected NPs: **A**: some selected 30 formula unit NPs calculated with DFT (spectra for A and N NPs have been vertically transposed by 150 and 300 km mol–1, respectively, for the sake of clarity). **B**: the 50 BC NP IR spectrum calculated with DFT.

Contributions from subsets of atoms are also reported (see Subsection 3.3.1). **C**: the 50 BC NP IR spectrum as calculated using DFT and using the Walker FF. **D**: all 104 NPs IR spectra calculated with the Walker FF. **E**: 418 units BC and 418 units A NPs IR spectra calculated using the Walker FF. The spectra for experimentally-synthetized crystalline forsterite and amorphous olivine are also reported for comparison.[35] These experimental spectra have been reproduced with the authors' permission.

Figure 11 A reports the IR spectra of a wide selection of 30 formula unit NPs including examples of BC (both translated and non-translated), A (amorphized at 1800 K and 2400 K) and N families. At such a small NP size, and using 10 cm^{-1} as FWHM, clearly we do not have only two distinct peaks typical of amorphous silicates.[1,2,50,51] Indeed, many individual small narrow peaks extending over a wide range of wavelengths can be easily distinguished. However, even though the individual peaks of the spectra for each NPs differ in their position, the overall profile of all spectra is quite similar. In particular, the IR spectral profiles of these NPs are broadly characterized by two distinct regions, namely the Si-O stretching between 8 to 12 μm and the O-Si-O bending between 13 to 18 μm. Silicate NPs at these sizes tend to show sharp spectral features due to the limited number of atoms, irrespectively of the amorphous/crystalline nature of the specific NP in question. Calculated IR spectra of even smaller olivine and pyroxene silicate nanoclusters have been also reported showing a similar behaviour.[52] The comparison of all the spectra in **Figure 11 A** suggests that small crystalline and amorphous silicate NPs with an olivinic $Mg_2Si_2O_4$ composition are indistinguishable by IR spectroscopy irrespective of their origin. Generally, the large number of distinct peaks can be attributed to the effect of the high surface to core ratio of these NPs and the subsequent effect that surface relaxation exerts on the core of the NP. This is well underlined by **Figure 11 B** which shows the contribution to the IR spectrum of the 50 BC NP with respect to different chemical species (*i.e.*, "surface shell" and "core" silicates and Mg cations). In the surface shell, SiO_4 units contribute to the whole spectrum, while Mg ions in this region involve modes from $\lambda > 17$ μm (~590 cm^{-1}). The contributions from bulk SiO_4 units are also present throughout the 8-20 μm (~1250-500 cm^{-1}) range, but to a minor extent.

As IR calculations using DFT are extremely expensive for NPs larger than 50 formula-units, the IR spectra of larger NPs were analyzed by means of FF calculations. The IR spectra of these NPs were calculated using the Walker FF, which provides a reasonable account of the IR peak positions of silicate NPs (see also SI, **Figures S8**-**S17**). **Figure 11 C** shows a comparison between the IR spectrum of the 50 BC NP as calculated using the Walker FF and DFT at a PBE/OlBS level. The IR spectrum from a CM-based FF calculation can only provide an approximation to the more accurate QM-based DFT-calculated spectrum, however, the overall FF description of the IR spectrum appears to still be fairly well captured. In particular, the spectrum of the 50 formula-units NP in both cases is comprised

of a wide range of features with two main regions: the Si-O stretching region around 10 μm and the O-Si-O bending region. While the FF calculation reproduces the 10 μm features very well, intensity at the O-Si-O region (*i.e.* ~13-16 μm) are less well captured and which seems to be shifted towards longer wavelengths with respect to the DFT-calculated IR spectrum. This behaviour mirrors what shown in the comparison of the Walker FF calculated spectrum of forsterite with corresponding DFT-calculated spectrum and that from experiment (see **Figure 1**), and is thus perhaps a systematic feature of IR spectra calculated using the Walker FF. Nevertheless, the qualitative broad and double peaked IR spectrum is well reproduced in both calculations, which in both cases clearly do not provide evidence for a highly crystalline NP.

Figure 11 D shows the full IR spectra for all the 104 formula unit NPs calculated using the Walker FF as illustrative examples. As for the 50 BC NP in **Figure 11 B**, the characteristic broad double peaked silicate profile is reproduced for all BC, A and N NPs. In particular, the spectra from the two BC and the two A NPs are almost identical, with very similar absolute intensities for the two main peaks. As the sizes are increased, the O-Si-O bending region appears to be less sharp and more featureless and becomes more similar to the typical features observed in the spectra of astrosilicates. This similarity is even more clear for the spectra of the largest 418 formula-units NPs, depicted in **Figure 11 E**, shown together with two experimental IR spectra for crystalline forsterite and amorphous olivine.[35] At this size, which corresponds to a NP diameter of ~4.6 nm, the BC NP IR spectrum is still dominated by the two broad silicate peaks and thus, like the A NP, spectroscopically non-crystalline. As previously discussed, the effects of surface relaxation are, up to at least a size of ~4 nm, clearly large enough to prevent the appearance of crystalline features in the IR spectra.

The N NPs show slight changes from the BC and A particles. The first noticeable change corresponds to the decreases of the intensities of both peaks. In addition, the O-Si-O peak is arguably shifted towards lower values. This effect is found in the spectra of all the N NPs (see **Figures S18**-**S26** of the SI file) and is probably the result of the formation of silicate polymerization and MgO segregation. The displacement of the O-Si-O band has previously been linked to the progressive change of silicate structure along the mineral series olivine-pyroxene-silica [9,10,53]

The broadened IR peaks exhibited by our NPs is a direct consequence of the (partial) loss of local and periodic crystalline order. For BC NPs which maintain much of their periodic crystalline order with respect to amorphous NPs (see **Figure 9**, left) the local structural disorder mainly occurs at the surface (*i.e.* surface relaxation) as shown **Figure 10**. For BC NPs the proportion of surface to core atoms could be a useful indicator of the extent of surface relaxation. We may assume, for example, that a necessary condition for a nanoparticle (NP) to exhibit a crystalline-like IR spectrum would be

that it has at least 50% of its atoms to be in relatively undisturbed crystalline positions. Using the SCA (see Subsection 3.2.1), we predicted that the energetic stability cross-over size between amorphous and crystalline NPs is ~12 nm diameter. For this NP size, the SCA provides us with an estimate of the ratio of surface to core atoms of only 24%. This is a lower bound as in real NPs the surface area is typically larger than that of a sphere and surface reconstruction of the outermost atoms can also disrupt sub-surface atomic ordering. Nevertheless, at this cross-over size and above it is highly probable that olivinic NPs have crystalline cores and that the reconstructed surface atom proportion is <50%, and thus we would more likely expect a crystalline-like IR spectrum. Conversely, for the largest NPs considered in our study the SCA predicts a significantly higher lower bound proportion of surface atoms of 60.5% for the 418 NPs and 79.3% for the 116 formula-units NPs. The high proportion of surface atoms in each case and the associated surface reconstruction is consistent with the non-crystalline IR spectra for these NPs. We also note that atoms in the bulk also contribute somewhat to broadening, as it is evident from the absence in the IR spectra from all NP models of significant features at wavelengths larger than ~24 μm, usually assigned to modes involving Mg cations in perfect crystalline silicates.[6] As such, even in the NP core, the positions of Mg and O atoms in the largest considered BC NPs cannot be considered as fully mirroring those of crystalline forsterite.

Clearly, the IR spectra of our larger NPs of all types are dominated by two broad features associated with Si-O stretching and O-Si-O bending modes. The peak wavelength, width and strength of these bands are related to the distribution of Si-O bond lengths and O-Si-O angles in each NP. For very narrow distributions of these quantities (as in crystalline forsterite) the associated IR bands will also be very narrow. For non-crystalline systems, the associated IR peaks will be related to the properties of the distributions of Si-O bonds and O-Si-O angles (*e.g.* broadness, maximum values). Clearly, we have similar types of 10 and 18 μm bands (i.e. position, width and intensity) for both relaxed BC NPs and amorphized NPs and we should thus expect that their Si-O bond lengths and O-Si-O angle distributions are similar. In the SI (see **Figures S27**-**S32**) we show these distributions for the BC, A and N 116 formula unit NPs clearly demonstrating their similarity, thus helping to underpin the similarity of the resultant IR peaks. We also note that the width of the Si-O stretching peak in our larger NPs ranges from 1.7 to 2.0 μm which is in line with typical ISM 9.710 μm peak widths.[54] Although consistent with observation, our calculations only deal with a very small selection of NP structures, sizes and compositions and the possible significance of this match should not be overstated.

As a consequence of the above-mentioned effects, the simulated NP spectra for all our larger NPs closely resemble those assumed to arise from amorphous cosmic silicates. Thus, contrary to the spectroscopic distinguishability of large crystalline and amorphous dust grains, Mg-rich olivinic nanograins (at least in the size range considered herein) cannot be classified as being in an amorphous or crystalline state only from their IR spectra, despite the fact that they can be explicitly and measurably shown to be structurally and energetically distinguishable.

3.3.2. *Temperature effect on simulated IR spectra*

To justify the extent of broadening (FWHM) applied to the individual harmonic frequencies in our computed IR spectra above, we also computed the IR spectra for the 104 BC and 80 BC NPs (as test cases) directly from finite temperature classical MD simulations at temperatures of 100 K and 400 K. As these calculations would be extremely computationally expensive to perform at a QM level, we employed the CM-based GULP codes for this analysis. Such calculations inherently incorporate anharmonic effects and thus provide a realistic measure of the temperature-induced broadening of spectral features. Details on the theoretical background to calculate such spectra can be found in the SI. The results for the 104 BC NP only are shown in **Figure 12**.

At a temperature of 100 K, the MD-based IR spectra show at least five discernable peaks in the 10-12 μm Si-O stretching region and three peaks in the 15-22 μm O-Si-O bending region. This corresponds well to the respective number of distinct peaks in each corresponding region of the 10 cm$_{-1}$ broadened harmonic spectrum (see lower spectra in **Figure 12**, left). Conversely, the 400 K MD-derived anharmonic spectrum has fewer discernible peaks in the Si-O wavelength region and only a single broad peak with two shoulders in the O-Si-O bending region. This spectrum better corresponds to a 20 cm$_{-1}$ broadened harmonic spectrum (see upper spectra in **Figure 12**, right).

From these results, we can conclude that when computing the IR spectra of NPs using the harmonic approximation, the applied broadening can be tuned to simulate temperature-induced anharmonic effects. Here, we find that a harmonic IR spectrum broadened by 10 cm$_{-1}$ provides a good approximation to the inherent broadening of an IR spectrum of a NP at ~100 K. All our harmonic spectra in **Figure 11** are broadened by 10 cm$_{-1}$ and thus roughly correspond to the temperatures that could be encountered in a number of astrophysical environments (*e.g.*, CS, protoplanetary disks, exoplanetary atmospheres, diffuse interstellar clouds). We further note that this analysis only corresponds to the effect of temperature on the IR spectrum of a single NP. A more detailed analysis should take into account large ensembles of NPs with different sizes and structures which will also tend to affect the discernable details in an observed IR spectrum.

We note that the small amount of broadening applied to our calculated harmonic frequencies results in a corresponding broadening of the wavelength peaks of ~0.1 μm. As such, the applied broadening mainly affects the number of resolved peaks in a spectrum, but does not significantly affect the overall broadness of features comprised of many summed peaks (as clearly seen in **Figure 12**). As such, the widths of our calculated Si-O and O-Si-O features are hardly affected by the choice of individual peak broadening.
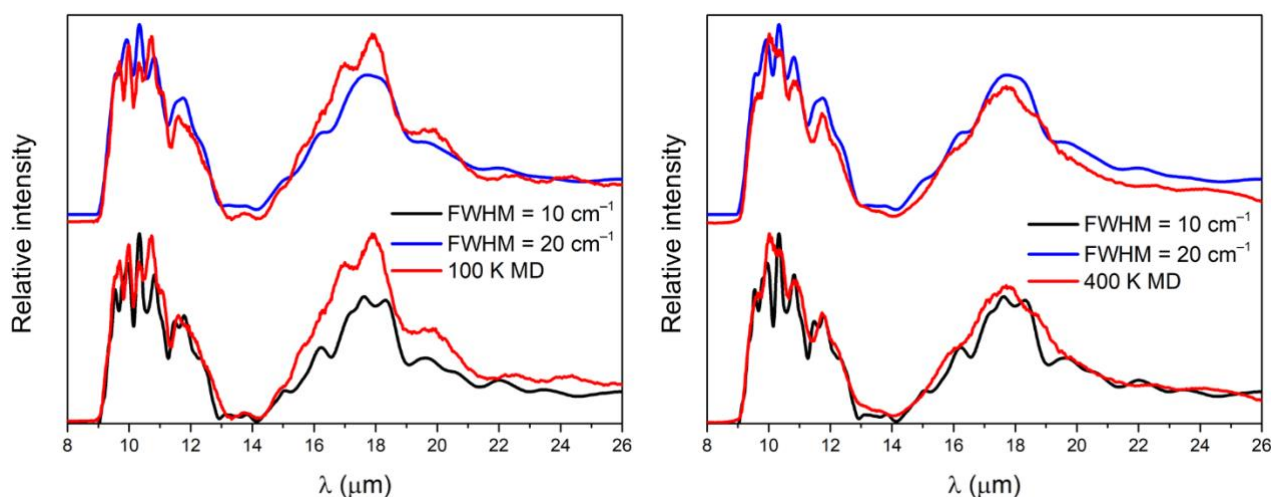

Figure 12 Comparison of the harmonic IR spectra for the 104 BC NP applying two different broadenings (FWHM = 10 cm$_{-1}$ in black and FWHM= 20 cm$_{-1}$ in blue), with the MD based IR spectra (red). The MD simulation temperature is set equal to 100 K (left) and 400 K (right).

4. CONCLUSIONS

In this work we provide a comprehensive study of the energetic, structural and IR spectroscopic properties of crystalline and non-crystalline Mg-rich olivine (Mg_2SiO_4) NPs possessing 10s to 1000s of atoms (from ~1 to ~5 nm in diameter). Bulk cut (BC) crystalline-like NPs were modelled using the top-down Wulff construction, while two kinds of non-crystalline NPs were studied: thermally annealed (amorphized, A) NPs based on the Wulff constructed cuts, and nucleated (N) particles grown by monomeric addition. While the amorphized and bulk cut NPs share some structural features similar to bulk crystalline forsterite (*e.g.* isolated SiO_4 units), the nucleated NPs show the presence of pyroxene-like chains and small MgO regions, and thus can be seen as partial solid mixtures. In terms of energetics, BC NPs are metastable with respect to annealed amorphous NPs, while nucleated NPs are higher in energy than both other NP types. In the bulk phase, however, crystalline forsterite is the most energetically stable phase. From the size-dependent energetic trends of the annealed and crystalline NPs, we tentatively estimate that the energetic stability cross-over size between these two NP families will occur for a NP size of ~12 nm diameter.

We have analysed the structures of our NPs in detail in order to evaluate the effects of amorphization by comparing three measures of crystallinity to assess local and periodic order. The displacements of silicon atoms were used to characterize the periodic order and demonstrated that the amorphous NPs are easily structurally differentiated as more disordered with respect to the crystalline BC NPs. From the analysis of the "average Mg coordination number" <Mg CN>, our local order descriptor, we show that the BC NPs have lower than bulk values due to surface effects, which cause a lowering of the Mg coordination. However, the A and N NPs show even lower <Mg CN> values due to their more disordered structures. Examining the spatially resolved local structural distortion of tetrahedral SiO_4 units in BC and A NPs we also confirm that: *i*) A-type NPs show a homogenous distribution of disorder throughout the whole NP, and *ii*) BC NPs show only significant local structural distortion at their surfaces. Due to the large surface to core atom proportions (> 50%) in the considered NPs the effect of surface relaxation on the IR spectra of BC NPs is found to be relatively large.

The IR spectra of the smallest NPs are composed of a large collection of distinct signals. As the NP size increases the IR spectra of all NP families show broader peaks in the characteristic ~10 and ~18 μm regions, in accordance with typical astronomical silicate IR spectra. Surprisingly, both thermally annealed structurally amorphous NPs and NPs relaxed from bulk crystalline cuts (with only significant disorder at their surfaces) show similar double peaked broad spectra. Indeed, from the calculated IR spectra, our larger BC and A NPs would be clearly judged as spectroscopically amorphous. This result implies that that it would be very difficult to accurately estimate the degree of crystallinity of nanosilicate grains in the ~1-5 nm diameter regime using IR spectroscopy alone. In contrast, the IR spectra from nucleated NPs arising from gas phase monomeric addition show some features that make them distinguishable from the A and BC NPs.

There are several astronomical implications to our results. First, the higher energetic stability of amorphous NPs with respect to their crystalline counterparts highlight the necessity to include such considerations in theoretical works of the formation of silicates in different environments. Here, however, further work is necessary to provide a more accurate estimate of the cross-over NP size for the amorphous to crystalline transition. Second, the IR spectra of maximally crystalline nanograins (*i.e.* BC NPs) having diameters of ~4.5 nm cannot be distinguished from the corresponding spectra of amorphous nanograins (*i.e*. A NPs). This surprising result may cast some doubts on the currently established upper limits of the fraction of crystalline silicate dust in the ISM based on observed IR spectra. If a large population of crystalline nanograins exists in the ISM, a traditional analysis would lead to their observed IR spectra being interpreted as showing the presence of amorphous grains. Generally, the existence of many highly crystalline nanograins could be hidden in IR spectra that are

usually taken to indicate only amorphous silicates. Although further studies are needed to evaluate the size regime where the IR spectra of crystalline and amorphous NPs eventually becomes distinguishable, our results may also provide support for preliminary results from X-ray absorption observations[49,55] which indicate a relatively large fraction of crystalline silicate dust in the ISM as compared to estimates based on analyses of IR spectra.[16]

5. ACKNOWLEDGEMENTS

6. AUTHOR INFORMATION

Corresponding authors

Stefan T. Bromley. E-mail: s.bromley@ub.edu, telephone: +34 93 403 9732

Piero Ugliengo. E-mail: piero.ugliengo@unito.it, telephone: +39 011 670 4596

Other authors

Lorenzo Zamirri. E-mail: lorenzo.zamirri@unito.it

Antoni Macià Escatllar. E-mail: tonimacia@gmail.com

Joan Mariñoso Guiu. E-mail: jmaringu11@alumnes.ub.edu

ORCID

Stefan T. Bromley: 0000-0002-7037-0475

Piero Ugliengo: 0000-0001-8886-9832

Lorenzo Zamirri: 0000-0003-0219-6150

Antoni Macià Escatllar: 0000-0002-3008-4554

Joan Mariñoso Guiu: 0000-0001-7154-8450

7. SUPPORTING INFORMATION

The Supporting Information (SI) file is organized into sections. S1: description of computational details. S2: technical details about the procedure we followed to generate bulk cut and amorphized NPs. S3: details of the calculations used to derive a realistic value of the full width at half maximum for the IR spectra. S4: plots of the harmonic IR spectra for all NPs. S5: Si-O bond distance and O-Si-O angle distributions for the 116 formula-units BC, A and N NPs. This SI file is also integrated with some other supporting material available online: Cartesian coordinates of all optimised NPs where we report the structure of each Ol NP in the XMOL format, and input and output files of our CRYSTAL (DFT) and GULP (Walker FF) calculations containing the computed IR intensities and frequencies of all NPs.

REFERENCES

(1)   Henning, T. Cosmic Silicates. *Annu. Rev. Astron. Astrophys.* **2010**, *48*, 21–46.

(2)   Henning, T. Cosmic Silicates - A Review. In *Solid State Astrochemistry*; Pirronello, V., Krelowski, J., Manicò, G., Eds.; Proceedings of the NATO Advanced Study Institute on Solid State Astrochemistry, 2000; pp 85–103.

(3)   Malfait, K.; Waelkens, C.; Waters, L. B. F. M.; Vandenbussche, B.; Huygen, E.; de Graauw, M. S. The Spectrum of the Young Star HD 100546 Observed with the Infrared Space Observatory. *Astron. Astrophys.* **1998**, *332*, L25–L28.

(4)   Hanner, M. S. The Silicate Material in Comets. *Space Sci. Rev.* **1999**, *90*, 99–108.

(5)   Waters, L. B. F. M.; Molster, F. J.; de Jong, T.; Beintema, D. A.; Waelkens, C.; Boogert, A. C. A.; Boxhoorn, D. R.; de Graauw, T.; Drapatz, S.; Feuchtgruber, H.; Genzel, R.; Helmich, F. P.; Heras, A. M.; Huygen, R.; Izumiura, H.; Justtanont, K.; Kester, D. J. M.; Kunze, D.; Lahuis, F.; Lamers, H. J. G. L. M.; Leech, K. J.; Loup, C.; Lutz, D.; Morris, P. W.; Price, S. D.; Roelfsema, P. R.; Salama, A.; Schaeidt, S. G.; Tielens, A. G. G. M.; Trams, N. R.; Valentijn, E. A.; Vandenbussche, B.; van den Ancker, M. E.; van Dishoeck, E. F.; van Winckel, H.; Wesselius, P. R.; Young, E. T. Mineralogy of Oxygen-Rich Dust Shells *Astron. Astrophys.* **1996**, *315*, L361–L364..

(6)   Molster, F. J.; Kemper, C. Crystalline Silicates. *Space Sci. Rev.* **2005**, *119*, 3–28.

(7)   Jäger, C.; Molster, F. J.; Dorschner, J.; Henning, T.; Mutschke, H.; Waters, L. B. F. M. Steps toward Interstellar Silicate Mineralogy. IV. The Crystalline Revolution. *Astron. Astrophys.* **1998**, *339*, 904–916.

(8)   Molster, F. J.; Waters, L. B. F. M.; Tielens, A. G. G. M. Crystalline Silicate Dust around Evolved Stars II. The Crystalline Silicate Complexes. *Astron. Astrophys.* **2002**, *240*, 222–240.

(9)   Jäger, C.; Dorschner, J.; Mutschke, H.; Posch, T.; Henning, T. Steps toward Interstellar Silicate Mineralogy VII. Spectral Properties and Crystallization Behaviour of Magnesium Silicates Produced by the Sol-Gel Method. *Astron. Astrophys.* **2003**, *408*, 193–204.

(10)   Speck, A. K.; Whittington, A. G.; Hofmeister, A. M. Disordered Silicates in Space: A Study of Laboratory Spectra of "Amorphous" Silicates. *Astrophys. J.* **2011**, *740*, 17pp.

(11)   Hallenbeck, S. L.; Nuth III, J. A.; Nelson, R. N. Evolving Optical Properties of Annealing Silicate Grains: From Amorphous Condensate to Crystalline Mineral. *Astrophys. J.* **2000**, *535*, 247–255.

(12)   Thompson, S. P.; Parker, J. E.; Tang, C. C. The 10 μm Band in Amorphous $MgSiO_3$: The Influence of Medium-Range Structure, Defects and Thermal Processing. *Astron. Astrophys. Astrophys.* **2012**, *545*, A60.

(13)   Demyk, K.; D'Hendecourt, L.; Leroux, H.; Jones, A. P.; Borg, J. IR Spectroscopic Study of Olivine, Enstatite and Diopside Irradiated with Low Energy H_+ and He_+ Ions. *Astron. Astrophys.* **2004**, *420*, 233–243.

(14)   Chiar, J. E.; Tielens, A. G. G. M. Pixie Dust: The Silicate Features in the Diffuse Interstellar Medium. *Astrophys. J.* **2006**, *637*, 774–785.

(15)   Fogerty, S.; Forrest, W.; Watson, D. M.; Sargent, B. A.; Koch, I. Silicate Composition of the Interstellar Medium. *Astrophys. J.* **2016**, *830*, 71 (11 pp).

(16)   Kemper, F.; Vriend, W. J.; Tielens, A. G. G. M. The Absence of Crystalline Silicates in the Diffuse Interstellar Medium. *Astrophys. J.* **2004**, *609*, 826–837.

(17)   Kemper, F.; Vriend, W. J.; Tielens, A. G. G. M. The Absence of Crystalline Silicates in the Diffuse Interstellar Medium. Erratum. *Astrophys. J.* **2005**, *663*, 534–534.

(18)   Li, M. P.; Zhao, G.; Li, A. On the Crystallinity of Silicate Dust in the Interstellar Medium. *Mon. Not. R. Astron. Soc.* **2007**, *382*, L26–L29.

(19)   Li, A.; Draine, B. T. On Ultrasmall Silicate Grains in the Diffuse Interstellar Medium. *Astrophys. J.* **2001**, *550*, L213–L217.

(20)   Kogut, A.; Banday, a. J.; Bennett, C. L.; Gorski, K.; Hinshaw, G.; Smoot, G. F.; Wright, E. L. Microwave Emission at High Galactic Latitudes. *Astrophys. J.* **1996**, *464*, L5–L9.

(21)   Draine, B. T.; Lazarian, A. Diffuse Galactic Emission from Spinning Dust Grains. *Astrophys. J.* **1998**, *494*, L19–L22.

(22)   Draine, B. T.; Lazarian, A. Electric Dipole Radiation from Spinning Dust Grains. *Astrophys. J.* **1998**, *508*, 157–179.

(23) Dovesi, R.; Saunders, V. R.; Roetti, C.; Orlando, R.; Pascale, F.; Civalleri, B.; Doll, K.; Harrison, N. M.; Bush, I. J.; D'Arco, P.; Llunel, M.; Causà, M.; Noël, Y.; Maschio, L.; Erba, A.; Rérat, M.; Casassa, S.. CRYSTAL17. User's Manual. 2018.

(24) Gale, J. D. GULP - A Computer Program for the Symmetry Adapted Simulation of Solids. *J. Chem. Soc. Faraday Trans* **1997**, *93*, 629.

(25) Plimpton, S. Fast Parallel Algorithms for Short-Range Molecular Dynamics. *J. Comput. Phys.* **1995**, *117*, 1–19.

(26) Perdew, J. P.; Burke, K.; Ernzerhof, M. Generalized Gradient Approximation Made Simple. *Phys. Rev. Lett.* **1996**, *77*, 3865–3868.

(27) van Duin, A. C. T.; Dasgupta, S.; Lorant, F.; Goddard III, W. A. ReaxFF: A Reactive Force Field for Hydrocarbons. *J. Phys. Chem. A* **2001**, *105*, 9396–9409.

(28) Walker, A. M.; Wright, K.; Slater, B. A Computational Study of Oxygen Diffusion in Olivine. *Phys. Chem. Miner.* **2003**, *30*, 536–545.

(29) Price, G. D.; Parker, S. C.; Leslie, M. The Lattice Dynamics and Thermodynamics of the Mg2SiO4 Polymorphs. *Phys. Chem. Miner.* **1987**, *15*, 181–190.

(30) Catlow, C. R. A.; Price, G. D. Computer Modelling of Solid-State Inorganic Materials. *Nature* **1990**, *347*, 243–247.

(31) Simons, J.; Joergensen, P.; Taylor, H.; Ozment, J. Walking on Potential Energy Surfaces. *J. Phys. Chem.* **1983**, *87*, 2745–2753.

(32) Banerjee, A.; Adams, N.; Simons, J.; Shepard, R. Search for Stationary Points on Surfaces. *J. Phys. Chem.* **1985**, *89*, 52–57.

(33) Baroni, S.; de Gironcoli, S.; dal Corso, A.; Giannozzi, P. Phonons and Related Crystal Properties from Density-Functional Perturbation Theory. *Rev. Mod. Phys.* **2001**, *73*, 515–562.

(34) Goumans, T. P. M.; Bromley, S. T. Efficient Nucleation of Stardust Silicates via Heteromolecular Homogeneous Condensation. *Mon. Not. R. Astron. Soc.* **2012**, *420*, 3344–3349.

(35) Yamamoto, D.; Tachibana, S. Water Vapor Pressure Dependence of Crystallization Kinetics of Amorphous Forsterite. *ACS Earth Sp. Chem.* **2018**, *2*, 778–786.

(36) Lamiel-Garcia, O.; Cuko, A.; Calatayud, M.; Illas, F.; Bromley, S. T. Predicting Size-Dependent Emergence of Crystallinity in Nanomaterials: Titania Nanoclusters versus Nanocrystals. *Nanoscale* **2017**, *9*, 1049–1058.

(37) Bromley, S. T.; Moreira, I. D. P. R. R.; Neyman, K. M.; Illas, F. Approaching Nanoscale Oxides: Models and Theoretical Methods. *Chem. Soc. Rev.* **2009**, *38* (9), 2657–2670.

(38) Bostrom, D. Single-Crystal X-Ray Diffraction Studies of Synthetic Ni−Mg Olivine Solid

Solution. *Am. Mineral.* **1987**, *72*, 965–972.

(39) Momma, K.; Izumi, F. VESTA 3 for Three-Dimensional Visualization of Crystal, Volumetric and Morphology Data. *J. Appl. Crystallogr.* **2011**, *44*, 1272–1276.

(40) Bruno, M.; Massaro, F. R.; Prencipe, M.; Demichelis, R.; De La Pierre, M.; Nestola, F. Ab Initio Calculations of the Main Crystal Surfaces of Forsterite (Mg_2SiO_4): A Preliminary Study to Understand the Nature of Geochemical Processes at the Olivine Interface. *J. Phys. Chem. C* **2014**, *118*, 2498–2506.

(41) Zamirri, L.; Corno, M.; Rimola, A.; Ugliengo, P. Forsterite Surfaces as Models of Interstellar Core Dust Grains: Computational Study of Carbon Monoxide Adsorption. *ACS Earth Sp. Chem.* **2017**, *1*, 384–398.

(42) Jacobs, M. H. G.; de Jong, B. H. W. S. An Investigation into Thermodynamic Consistency of Data for the Olivine, Wadsleyite and Ringwoodite Form of $(Mg,Fe)_2SiO_4$. *Geochim. Cosmochim. Acta* **2005**, *69*, 4361–4375.

(43) Johnston, R. L. *Atomic and Molecular Clusters*; CRC Press, Taylor & Francis Group, 2002.

(44) Viñes, F.; Lamiel-Garcia, O.; Illas, F.; Bromley, S. T. Size Dependent Structural and Polymorphic Transitions in ZnO: From Nanocluster to Bulk. *Nanoscale* **2017**, *9*, 10067–10074.

(45) Suh, K. W. Crystalline Silicates in the Envelopes and Discs around Oxygen-Rich Asymptotic Giant Branch Stars. *Mon. Not. R. Astron. Soc.* **2002**, *332*, 513–528.

(46) Gail, H.-P.; Sedlmayr, E. Mineral Formation in Stellar Winds. I. Condensation Sequence of Silicate and Iron Grains in Stationary Oxygen Rich Outflows. *Astron. Astrophys.* **1999**, *347*, 594–616.

(47) Molster, F. J.; Yamamura, I.; Waters, L. B. F. M.; Nyman, L.-A.; Kaufl, H.-U.; de Jong, T.; Loup, C. IRAS 09425−6040: A Carbon Star Surrounded by Highly Crystalline Silicate Dust. *Astron. Astrophys.* **2001**, *366*, 923–929.

(48) Gail, H. P.; Sedlmayr, E. Inorganic Dust Formation in Astrophysical Environments. *Faraday Discuss.* **1998**, *109*, 303–319.

(49) Zeegers, S. T.; Costantini, E.; de Vries, C. P.; Tielens, A. G. G. M.; Chihara, H.; de Groot, F.; Mutschke, H.; Waters, L. B. F. M.; Zeidler, S. Absoption and Scattering by Interstellar Dust in the Silicon K-Edge of GX5-1. *Astron. Astrophys.* **2017**, *599*, A117 (11 pp).

(50) Meeus, G.; Waters, L. B. F. M.; Bouwman, J.; van den Ancker, M. E.; Waelkens, C.; Malfait, K. ISO Spectroscopy of Circumstellar Dust in 14 Herbig Ae/Be Systems: Towards an Understanding of Dust Processing. *Astron. Astrophys.* **2001**, *365*, 476–490.

(51) Draine, B. T. Interstellar Dust Grains. *Annu. Rev. Astron. Astrophys.* **2003**, *41*, 241–289.

(52) Macià, A.; Lazauskas, T.; Woodley, S.; Bromley, S. T. Structure and Properties of Nanosilicates with Olivine $(Mg_2SiO_4)_N$ and Pyroxene $(MgSiO_3)_N$ Compositions. *ACS Earth Sp. Chem.* **2019**. https://doi.org/10.1021/acsearthspacechem.9b00139

(53) Ossenkopf, V.; Henning, T.; Mathis, J. S. Constraints on Cosmic Silicates. *Astron. Astrophys.* **1992**, *261*, 567–578.

(54) Shao, Z.; Jiang, B. W.; Li, A.; Gao, J.; Lv, Z.; Yao, J. Probing the 9.7 μm Interstellar Silicate Extinction Profile through the Spitzer/IRS Spectroscopy of OB Stars. *Mon. Not. R. Astron. Soc.* **2018**, *478*, 3467–3477.

(55) Zeegers, S. . T.; Costantini, E.; Rogantini, D.; de Vries, C. P.; Mutschke, H.; Mohr, P.; de Groot, F.; Tielens, A. G. G. M. Dust Absorption and Scattering in the Silicon K-Edge. *Astron. Astrophys.* **2019**, *627*, A16 (18 pages).

Table of contents figure: